

ASTEROID TAXONOMY FROM CLUSTER ANALYSIS OF SPECTROMETRY AND ALBEDO

PREPRINT

Max Mahlke¹, Benoit Carry¹, and Pierre-Alexandre Mattei²

¹Université Côte d'Azur, Observatoire de la Côte d'Azur, CNRS, Laboratoire Lagrange, France

²Université Côte d'Azur, Inria, Maasai project-team, Laboratoire J.A. Dieudonné, UMR CNRS 7351, France

ABSTRACT

The classification of the minor bodies of the Solar System based on observables has been continuously developed and iterated over the past 40 years. While prior iterations followed either the availability of large observational campaigns or new instrumental capabilities opening novel observational dimensions, we see the opportunity to improve primarily upon the established methodology. We develop an iteration of the asteroid taxonomy which allows for classification of partial and complete observations, i.e. visible, near-infrared, and visible-near-infrared spectrometry, and which re-introduces the visual albedo into the classification observables. The resulting class assignments are given probabilistically, enabling to quantify the uncertainty of a classification. We build the taxonomy based on 2983 observations of 2125 unique asteroids, representing an almost tenfold increase of sample size compared with the previous taxonomy. The asteroid classes are identified in a lower-dimensional representation of the observations using a Mixture of Common Factor Analyzers model. We identify 17 classes split into the three complexes C, M, and S, including the novel Z-class for extremely-red objects in the Main Belt. The visual albedo information resolves the spectral degeneracy of the X-complex and establishes the P-class as part of the C-complex. We present a classification tool which computes probabilistic class assignments within this taxonomic scheme from asteroid observations, intrinsically accounting for degeneracies between classes based on the observed wavelength region. The ability to classify partial observations and the re-introduction of the visual albedo into the classification provide a taxonomy which is well suited for the current and future datasets of asteroid observations, in particular provided by Gaia, the MITHNEOS-, and the SPHEREx surveys.

1 INTRODUCTION

The minor planets of the Solar System exhibit a wide range of surface compositions as outcome of their diverse formation histories. Mineralogical insights into the Main Asteroid Belt gained from observing the bodies' exteriors serve to constrain the dynamic-evolution scenarios of our planetary environment (Morbidelli et al. 2015) as well as to establish relationships in asteroid families (Masiero et al. 2015) and to identify the parent bodies of the members of the meteorite collection (Burbine et al. 2002; Granvik and Brown 2018). The conclusion of a static Solar System formation history (Gradie and Tedesco 1982) has since been discarded in favour of a dynamical one (Gomes et al. 2005; Morbidelli et al. 2005; Tsiganis et al. 2005) following the increasing resolution of the compositional distribution of asteroids in the Main Belt and in near-Earth orbits thanks to a growing number of minor bodies characterized by dedicated observational efforts (e.g. Xu et al. 1995; Bus and Binzel 2002a; Devogèle et al. 2019). Nowadays, the majority of the mass in the Main Belt is thought to have been dynamically implanted during a later evolutionary stage of the Solar System (Gradie and Tedesco 1982; DeMeo and Carry 2014), including some of the largest members of the Main Belt (Bottke et al. 2006; De Sanctis et al. 2015; Vokrouhlický et al. 2016; Ribeiro de Sousa et al. 2022). Evidence of a dichotomous meteorite population further strengthens this interpretation of a large compositional variability among minor bodies as result of early-stage formation processes in the Solar System (Warren 2011).

To describe the compositional distribution, a classification scheme based on the observable features of asteroids is required. A common device used to aid the interpretation of observations is asteroid taxonomy. Taxonomic classification refers to the grouping of objects with shared characteristics (Candolle 1813). For asteroids,

these characteristics are the observable surface properties such as the absorption bands imprinted into their reflectance spectra or the surface albedos. The implicit assumption is that the observables are related to the minor planets' surface mineralogy (Gaffey and McCord 1979), though this is not a prerequisite for a practical taxonomy.

Schemes for the compositional classification of minor planets have been devised and iterated over regularly since the 1970s (e.g. Chapman et al. 1971; McCord and Chapman 1975; Bowell et al. 1978). The initial division into carbonaceous C-types and siliceous S-types was readily apparent in different observables even for a low number of observed objects and limited observational detail. However, as an increasing number of smaller objects is observed, the underlying continuum distribution between these complexes is revealed (Bus and Binzel 2002b).

The most commonly used taxonomies for minor bodies are the Tholen (Tholen 1984) and the Bus-DeMeo system (Bus and Binzel 2002b; DeMeo et al. 2009). While the latter offers a feature-based classification which encompasses a wide range of the variability observed in spectral observations and has been adapted both to visible- and *near-infrared* (NIR) photometric observations (Carvano et al. 2010; DeMeo and Carry 2013; Popescu et al. 2018), the former has not been fully replaced in part due to two advantages of the used asteroid observables; the visual albedo p_V as well as spectrophotometric observations down to *ultra-violet* (UV) wavelengths. Both features increase in particular the resolution of classes which only show faint features in the visible- and NIR wavelength regimes.

In this work, we aim to improve upon the existing taxonomic schemes for minor bodies in three aspects. First, we introduce a method which enables to classify both complete and partial observations. This offers consistent class definitions across the

visible-near-infrared (VisNIR) region. Second, the visual albedo p_V is re-introduced into the taxonomy observables, solving the degeneracy of the X-complex as primary consequence. Third, asteroids are classified in a probabilistic model, yielding a vector of class probabilities rather than a definite class assignment, which enables to identify taxonomic outliers and transitional populations.

In Sect. 2, we outline the collection of the observational data used in this study, as well as the methodological advancement of the clustering strategy with respect to previous taxonomies. Sect. 3 outlines the clustering results and the strategy of identifying compositional classes. These classes are then discussed in detail in Sect. 4. In Sect. 5, we investigate degeneracies between the classes in this taxonomy and compare the classifications of asteroids in this study to the ones in the literature. A tool to classify asteroid observations in the framework of this taxonomy is presented. Finally, we draw conclusions and give an outlook in Sect. 6.

2 METHOD

In this section, we describe the compilation and preprocessing of the asteroid spectra and albedos for the cluster analysis, followed by a description of the issues that arise when working with partial observations, i.e. “missing data”. After motivating the split of the dataset into clustering and classification data, the section concludes with a description of our approach to the dimensionality reduction and clustering problem at hand.

2.1 Input Data

2.1.1 Selecting the Observables

The selection of asteroid observables which are included in a taxonomical system is a crucial decision in its design. A broad set of observables ensures its applicability to a large number of asteroids and high compositional resolution, however, it complicates the derivation of the classification scheme and limits the number of available observations as only the intersection in terms of observed asteroids can be considered when combining different datasets.¹ This first led Tholen (1984) to apply the albedo only in a secondary classification step before the observable was completely dropped by Bus and Binzel (2002b).

As one of our main goals for this iteration of the taxonomy is the possibility to classify partial observations, we are a priori accepting gaps in the input data and are thus not limiting the sample size when combining datasets and can use the union rather than the intersection of observations. Nevertheless, while we at first considered a classification system based around spectrometric and photometric observations as well as visual albedos and phase curve coefficients, we noticed that the latter of both observable pairs did not add to the compositional resolution of the resulting scheme as they are effectively low-resolution versions of the former (DeMeo and Carry 2013; Shevchenko et al. 2016; Mahlke et al. 2021). Therefore, we choose to build the taxonomy from asteroid VisNIR spectra and visual albedos.

¹In machine learning literature, the observables used to identify groups in the input data are referred to as *features*, while the observations are referred to as *samples*. The *input data* is a matrix spanned by the features as columns and the samples as rows.

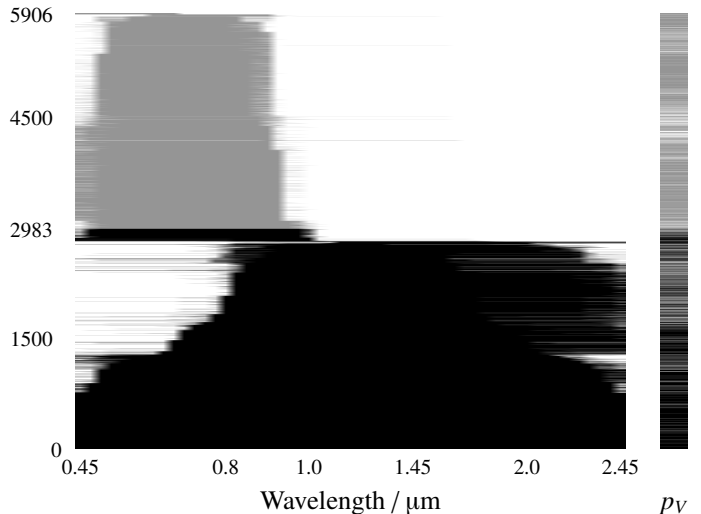


Figure 1: The input data is shown as matrix with the columns representing the asteroid observables, i.e. the spectral wavelength bins and the visual albedo p_V and each row representing one observation. The cells are white if the corresponding value was not observed. Black cells indicate samples which are used in the clustering analysis, gray cells give samples which are classified but not used to build the taxonomy itself. The matrix is sorted by increasing completeness of the asteroid spectra from top to bottom.

2.1.2 Spectra

Spectrometric observations are the most compositionally informative asteroid features accessible via remote sensing. In preparing this work, we focused both on building a large repository of asteroid spectra as well as curating the data. In total, we acquired over 7500 spectra from online repositories, archived publications, and directly from the observers. After several iterations of visual inspection and rejection of low-quality data and duplicated observations, 6038 spectra of 4526 unique asteroids remained. About 50 % of spectra cover the visible wavelength range only, while the sample of VisNIR spectra is about three times as large as in DeMeo et al. (2009), refer to Fig. 1.

The collection of spectra is heterogeneous in numerous aspects, including but not limited to their wavelength coverage, resolution, and sampling patterns. However, a consistent sampling pattern between all spectra is required for the following numerical analyses. We define this pattern in close resemblance to the one used by DeMeo et al. (2009), though we choose to halve the sampling step size in the visible wavelength range as we find that possible superpositions of absorption features due to mafic minerals around 1 μm are better described by the finer sampling. The chosen sampling pattern is

$$\lambda_S \in \{0.45, 0.475, 0.50, \dots, 1.0, 1.025, 1.05, 1.10, 1.15 \dots, 2.40, 2.45\} \mu\text{m}, \quad (1)$$

totaling 53 wavelengths. In the following cluster analysis, each of these wavelengths represents one *data dimension*.

Before resampling the spectra, we apply a filter (Savitzky and

Golay 1964) to smoothen e.g. telluric absorption features present in the spectra. The filter consists of applying least-squares fits of polynomials to a window of adjacent datapoints. The window size in units of datapoints and the degree of the polynomial dictate the amount of smoothing that is applied. We set these two parameters for each spectrum separately by visual inspection of the results. The smoothened spectra are then linearly interpolated and resampled to the pattern in Eq. (1). We then transform the spectra using the natural logarithm, which serves to approximate a zero-mean and uniform-standard-deviation of the input spectra as they are generally normalised to unity at either $0.55 \mu\text{m}$ or $1.25 \mu\text{m}$. This “standardisation” transform is generally beneficial to clustering and dimensionality reduction methods (Bouveyron et al. 2019).

The inclusion of missing data into the analysis poses a novel challenge when it comes to normalizing the spectral data. The common approach of multiplicatively setting the reflectance to unity at a shared wavelength is not possible as no single wavelength is shared among all spectra, as can be seen in Fig. 1. Furthermore, this approach would artificially decrease the variance in the wavelength chosen for normalization and the neighbouring wavelength bins, causing the subsequent clustering analysis to effectively ignore the normalization region.

Instead, we prepare the spectra in a way which benefits the following analysis most by employing a *Gaussian mixture model* (GMM). We assume that each spectrum can be written αy , where $\alpha \in \mathbb{R}$ is a normalisation constant that depends on the considered spectrum, and $y \in \mathbb{R}^{52}$ is a normalised spectrum. Further assuming that y follows a mixture of k log-normal distributions with diagonal covariances, all parameters of the models can be estimated from an incomplete data set via an expectation-maximisation algorithm (Dempster et al. 1977). This allows in particular to estimate the normalisation constants of all spectra, and to finally normalise them. By trial and error, we find that $k = 30$ mixture components result in a satisfying normalization. As outlined in Sect. 2.2, the assumption of a normal distribution of the input samples in data space is also made in the clustering analysis.

Finally, we note that DeMeo et al. (2009) remove the slope component of the spectra to decrease the influence of space weathering on the taxonomy as well as to increase the depth of features present in the data. We cannot do this due to the missing data, however, we consider the presence of spectral-weathering effects in the taxonomy a beneficial rather than unfavourable aspect, as we further outline in Sect. 4.

2.1.3 Albedo

The visual albedos used in this study were compiled for the IMCCE’s *Solar system Open Database Network* (SsODNet,² Berthier et al., in prep.). The main contributors in this compilation are the *Infrared Astronomical Satellite* (IRAS) (Tedesco et al. 2002), the *Wide-field Infrared Survey Explorer* (WISE) (Masiero et al. 2011), AKARI (Usui et al. 2011), and Spitzer (Trilling et al. 2016). We use the SsODNet service to collect 4704 albedo measurements for 3544 asteroids of which we have spectral observations using the rocks³ python-interface (Berthier et al., in prep.).

When possible, we make use of several albedo measurements per

²<https://ssp.imcce.fr/webservices/ssodnet/>

³<https://rocks.readthedocs.io>

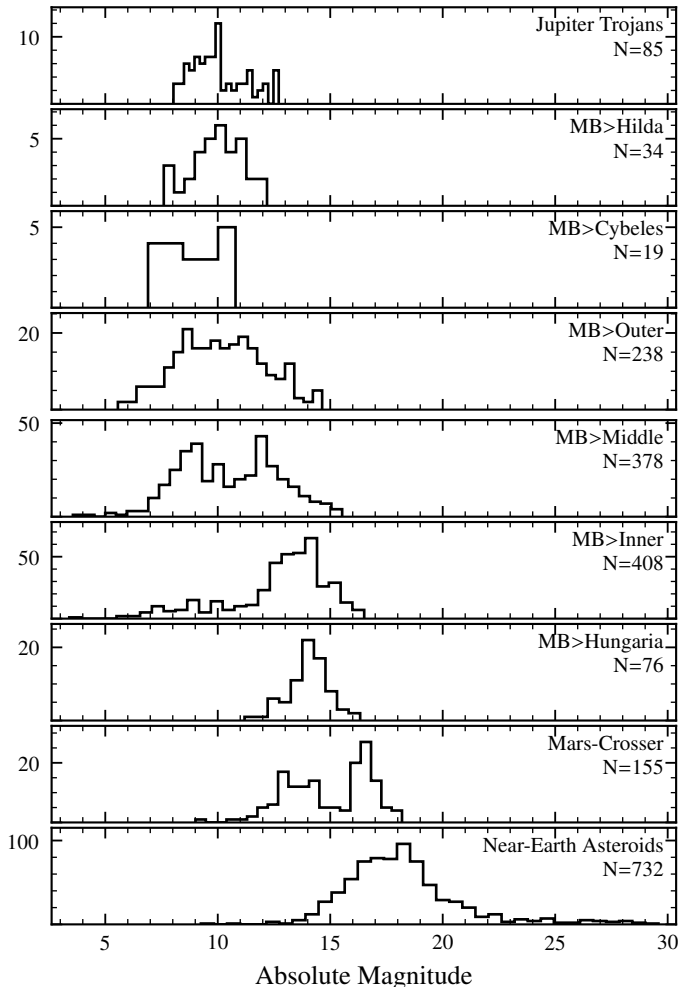


Figure 2: The distribution of the 2125 unique asteroids in the dataset used to build the taxonomy over orbital class and absolute magnitude. MB refers to the Main Belt. The number N of asteroids in the orbital population is given below each orbital class. Note that the binsize of the histograms varies with N .

asteroid when combining the input features, refer to Sect. 2.1.4. To get the most accurate available value for each asteroid, we first compute the albedo based on the weighted averages of the asteroid’s diameter and absolute magnitude provided by SsODNet following Harris and Lagerros (2002). These averages consist of the subjectively best available observations, refer to Berthier et al., in prep. In a second step, we compute the weighted mean of any albedo measurement available in the literature for the given asteroid and use this value as second available albedo observation in the input data. Finally, the non-aggregated albedo observations are appended as additional available measurements.

As for the spectra, we aim to have Gaussian distributions in the albedo data. Wright et al. (2016) shows that the distribution of albedos follows a double-Rayleigh distribution with a dark peak and a bright peak. To get a Gaussian distribution, we pass the log 10-transform of the albedos to the clustering algorithm after limiting all albedo values to the interval $[0.01, 1)$. Note that the albedo represents a single data dimension in the following analysis, compared to the 53 spectral data dimensions.

2.1.4 Merging of Data Samples

Previous taxonomies were derived based on photometry or spectrometry from a single dataset, e.g. the *Eight Color Asteroid Survey* (ECAS) (Zellner et al. 1985) for Tholen (1984) or the *Small Main-Belt Asteroid Spectroscopic Survey* (SMASS) (Xu et al. 1995) for Bus and Binzel (2002b). Individual observations of a single asteroid were combined in these datasets to give the single best-possible observation. In this work, we do not combine the observations as they come from numerous different sources. As such, 549 of 2125 asteroids have more than one observation in the input data.

When merging the asteroid spectra and albedos observations for each asteroid, we aim to create as many complete rows as possible. The array of albedo values is merged with the asteroid’s spectral values in order of most complete observations. If there are more albedo observations than spectra, we discard the remaining values. We further set an upper limit of 5 spectra for each asteroid, removing any excess ones in order of the least amount of observed wavelength bins. Many spectra of a single asteroid may cause artificial clusters or trends in the resulting taxonomy. This reduces the amount of available spectra from 6038 to 5906. Figure 1 shows the final matrix of observations, colour-coded to differentiate partial and complete observations.

2.1.5 Clustering versus Classification

When clustering the entire input dataset described above with the method outlined below, we note a population of clusters which contains mostly visible-only spectra. The intuitive explanation of these clusters is that when computing dimensionality reduction and projecting the spectra into a lower dimensional space, they will be distributed over a smaller volume than the VisNIR spectra due to their large degree of missing information. This artificial accumulation of input data in the latent space disturbs the identification of real clusters in the data. We therefore set an upper limit of 60 % of missing values per spectrum to be included into the clustering input data, which includes 2983 of the 5906 samples in the input data, refer to Fig. 1. The remaining 2923 are not used to derive the taxonomy, instead, they are classified in the resulting scheme and used to cross-validate the classification, as outlined in Sect. 5. In Fig. 2, we display the distribution of the 2125 unique asteroids in the data which we use to derive the taxonomy with in the sample over orbital classes and absolute magnitude.

2.1.6 Data availability

The dataframe containing the input data samples, asteroid meta-data, and the resulting classifications as outlined in the next sections is available at the *Centre de données astronomiques de Strasbourg* (CDS).⁴

2.2 Dimensionality Reduction and Clustering

The derivation of a taxonomy falls into the realm of unsupervised machine learning. In the context of minor bodies, the approach consists of two steps: dimensionality reduction followed by clustering. Previous taxonomies have predominantly chosen *Principal Component Analysis* (PCA) for the former and

visual clustering for the latter part. Given our goals for this new iteration of the current taxonomy as stated in Sect. 1, we need to evolve the established method, in particular to allow for the classification of partial observations. In the following, we outline this method evolution, which arises naturally when challenging the PCA method with the requirements of our input data and the prior knowledge from previous taxonomies. The description of the resulting model is kept concise, the reader is referred to Tipping and Bishop (1999), Baek et al. (2010) and Montanari and Viroli (2010) for detailed explanations as well as Casey et al. (2019) for an example application of the same model in the field of stellar physics.

2.2.1 Dimensionality Reduction

The necessity of dimensionality reduction derives mainly from the spectrometric observations, where each bin of the sampling pattern represents one of 54 data dimensions. Clustering in such high-dimensional space is not feasible as any model would be over-parametrized given the limited sample size of the input data. Reducing the dimensionality of the observed data space is achieved by building linear combinations of the observed variables, referred to as *latent variables*,⁵ and projecting the input data into the space spanned by the latent variables, referred to as *latent space*.

We assume that we have N observations of a p -dimensional observable. The input data \mathbf{Y} is thus of shape $N \times p$, denoted as $\mathbf{Y}_{N \times p}$.⁶ PCA can be described as eigendecomposition of the covariance matrix $\Sigma_{p \times p}$ of \mathbf{Y} ,

$$\mathbf{W}^T \Sigma \mathbf{W} = \Lambda, \quad (2)$$

where \mathbf{W} and Λ are the eigenvectors and -values of Σ (Pearson 1901). Expressing the p -dimensional Σ by the q -eigenvectors corresponding to the largest eigenvalues of Σ where $q < p$ leads to dimensionality reduction while retaining the largest possible amount of variance within the data. The lower-dimensional representation $\mathbf{Z}_{N \times q}$ of the input data \mathbf{Y} is given by the matrix product of \mathbf{Y} with the matrix of the subset of eigenvectors $\mathbf{W}_{p \times q}$. In the following, we denote \mathbf{W} as *latent components* and \mathbf{Z} as *latent scores*.

PCA does not allow for missing data as it relies on the eigendecomposition of Σ . This limitation is overcome by reformulating PCA as a latent generative variable model. In essence, while computing the latent components and scores from the input data, we are making the assumption that there exists a Gaussian-distributed variable z in the latent space which causes the variance observed in the higher-dimensional data, i.e. that the resulting latent scores are normal distributed. A general model of this approach can be expressed as (Tipping and Bishop 1999)

$$\mathbf{Y} = \mathbf{f}(\mathbf{Z}, \mathbf{W}) + \epsilon, \quad (3)$$

where f is a function of the latent scores \mathbf{Z} and the latent components \mathbf{W} and $\epsilon_{p \times p}$ is a noise matrix independent of \mathbf{Z} . The reformulation of PCA in this model framework is referred to

⁵Latent can here be understood as synonym for *hidden* or *underlying*, as these variables are not directly observable.

⁶In the following, we state the shape of the tensors in this manner when we first introduce them, and drop the notation afterwards.

⁴[\[url_placeholder\]](#)

as *probabilistic PCA* (PPCA) (Tipping and Bishop 1999). The model parameters are fit using an expectation-maximisation algorithm (Dempster et al. 1977) and, in case the input data is complete, gives the same solution as the conventional PCA.

PPCA assumes that the noise matrix ϵ is isotropic, i.e. all data dimensions carry the same noise. This is not necessarily the case for our observations, the uncertainties between visible and NIR spectra may differ from one another as well as from the one of the visual albedo. *Factor Analysis* (FA) is another latent generative variable model analogous to PPCA except that the noise matrix ϵ is assumed to be diagonal rather than isotropic (Rubin and Thayer 1982). The noise matrix is referred to as *uniqueness* as it captures the variance which is unique to each data dimension, effectively decoupling the measurement uncertainties from the data covariance.

In FA, the observations Y are modeled as

$$Y = \mu + WZ + \epsilon, \quad (4)$$

where $\mu_{p \times 1}$ is a p -dimensional vector containing the mean values of Y along the feature dimensions, W is the matrix of the latent components as above, and ϵ is a diagonal Gaussian noise matrix, $\epsilon \sim \mathcal{N}(\mathbf{0}, \Psi)$, where $\Psi_{p \times p}$ is diagonal. The latent variables Z follow a normal distribution with zero mean and unit covariance, $Z \sim \mathcal{N}(\mathbf{0}, I)$. The model parameters can be determined by a maximum-likelihood approach even in case of missing data, under the assumption that the data is missing-at-random, i.e. its probability to be missing is independent of its value (Little and Rubin 2019).

2.2.2 Clustering

Using the FA model given in Eq. (4), we assume that the distribution of the latent scores, i.e. the asteroid observations mapped into the latent space, follows a single Gaussian distribution. However, we know a priori from the previous taxonomic efforts that this is not the case; the C- and S-complexes form separate distributions and endmember classes such as A, K, and V follow separate trends in the latent scores (refer to Figure 2 in DeMeo et al. (2009)). Instead of a single Gaussian, we therefore model the data as a mixture of g Gaussian distributions, an approach which is referred to as *Mixture of Common Factor Analysers* (MCFA, Baek et al. 2010) in the case where the model components are fit in the same latent space as is the case here. MCFA can be expressed as specialization of the FA model in Eq. (4) using (Baek et al. 2010)

$$\begin{aligned} \mu_i &= \mathbf{A}\xi_i, \\ \Sigma_i &= \mathbf{A}\Omega_i\mathbf{A}^T + \mathbf{D}, \end{aligned} \quad (5)$$

where $i \in (1, \dots, g)$. \mathbf{A} is the common subspace of the mixture components, i.e. the matrix of latent components, ξ_i is the mean value of the i th mixture components in latent space and Ω_i its variance. The noise variance matrix \mathbf{D} retains its definition as above, meaning that all mixture components share the same noise.

In MCFA, dimensionality reduction and clustering are achieved concurrently during the model training. Starting from an initial set of model parameters as outlined in Sect. 3.1.2, at each training epoch, this model searches for the q -dimensional latent space and partitions the input samples into g components which give the

most likely projection of the input data assuming that it follows the mixture of g Gaussian distributions in the reduced space. The hyperparameters in the model are the number g of clusters and the number q of latent components.

2.3 Model Implementation and Availability

Implementations of the MCFA mixture-model approach are available in the R programming language⁷ by Baek et al. (2010) and in the python language⁸ by Casey et al. (2019). Nevertheless, we chose to write an alternative implementation in python as the implementation by the latter imputes the missing data via mean imputation before training the model using an expectation-maximisation algorithm. Mean imputation is not appropriate for our dataset as we know that the spectra of different asteroid classes may appear entirely different in terms of absorption features and slope. Inserting the mean column value in each empty cell does thus not represent the missing data well. Instead, we use the tensorflow library (Abadi et al. 2015) to implement a stochastic gradient descent learning strategy which maximizes the log-likelihood of the model given the *observed* data only, which is statistically sound under the missing-at-random assumption (Little and Rubin 2019), contrarily to using mean imputation. The stochastic gradient descent is of particular interest here as it estimates the model parameters based on batches of the input data, meaning that it can scale easily with an increasing number of observations. This MCFA implementation is independent from the taxonomy itself and may be applied in different studies. The implementation and documentation are available online.⁹

3 RESULTS

In this section, we present the results of fitting the MCFA model outlined in Sect. 2.3 to the input dataset described in Sect. 2.1. After depicting the latent space and the structure of the latent dimensions, we explain how the asteroid classes building this taxonomy are derived from the modelled Gaussian clusters.

3.1 Model Fit

3.1.1 Parameters

We choose to cluster the asteroid observations in $q = 4$ latent dimensions using $g = 50$ Gaussian clusters. Both numbers are selected from a wide range of values after assessing the resulting model fits. Larger values retain and describe more variability in the data while, at the same time, increasing the number of free parameters in the model, hence, a trade-off is made in both cases. The model fits obtained with 4 or 5 latent factors were comparable in terms of captured variability in the cluster, thus we opted for the smaller number of model parameters.

The large initial number of 50 clusters accounts for the model assumption of Gaussianity in the latent space. We have no reason to expect a Gaussian distribution of the asteroid classes, therefore, we model them as superposition of one or more Gaussian clusters. The modelled clusters are later joined and mapped to build the asteroid classes using a one-to-many relationship and following a decision tree.

⁷<https://github.com/suren-rathnayake/EMMIXmfa>

⁸<https://github.com/andycasey/mcfa>

⁹<https://github.com/maxmahlke/mcfa>

3.1.2 Initialization and Training

The latent loadings and cluster assignments of each observation have to be initialized at the start of the gradient descent algorithm to train the MCFA model. The initialization dictates the global position in the Hamiltonian which is sampled by the training and thus has a significant impact on the final result.

A practical issue when reducing the dimensionality of asteroid data made up by different observables is the feature weighting. In our case, the spectra contribute 53 data dimensions compared to the single dimension of the albedo. The summed variance in the former is much larger than the variance in the latter, resulting in a negligible contribution of the albedo to the latent space computation which does not reflect its actual information content. Tholen (1984) therefore chose not to include the albedo into the dimensionality reduction, using it in a subsequent manual clustering step instead. We employ an alternative strategy outlined below which allows us to account for the albedo *while* building the latent space.

We initialize the latent loadings using PPCA. This approach has two advantages: (1) the latent loadings are set to the axes of largest variance in the data, ensuring a high resolution in the latent space, and (2) PPCA is variant to feature scaling, i.e. data dimensions are weighted with respect to their variance when computing the dimensionality reduction. An effective way to increase the importance of the albedo information is hence to increase the variance of albedo values by some transformation prior to model training. We achieve this by means of the \log_{10} transformation described in Sect. 2.1.3, which increases the variance in the albedo dimension by a factor of 6.8. During the gradient-descent model training, we monitor the log-likelihood of the model given the data. As opposed to PPCA, MCFA is invariant to factor scaling, which leads to a decrease in the albedo loadings with each training step. Therefore, we do not train until the model has fully converged, instead stopping the training when a good balance between the weight of the albedo and of the spectra has been achieved. This subjective choice of training epochs is a concession we make to the challenge of combining different observables in the same model.

The latent cluster memberships are initialized by fitting a Gaussian mixture model with 50 components to the principal scores of the PPCA and assigning each sample to its most probable cluster. We train the MCFA model on the 2983 observations of 2125 unique asteroids as outlined in Sect. 2.1.4.

3.2 Latent Space

The latent components resulting from the model training are depicted in Fig. 3, with the spectral loadings given on the left hand side and the albedo loadings on the right hand side. The absolute value of a loading indicates the degree to which the latent component responds to variance in the corresponding data dimension. Positive loadings lead to an increase in the latent scores z with increasing value in the data dimension, negative values to a decrease in z . The latent scores Z are essentially a vector product of the input data with the latent components.

The spectral loadings in Fig. 3 resemble different mineralogical features commonly present in asteroid spectra. The first component approximates a positive slope,¹⁰ with an inflection point

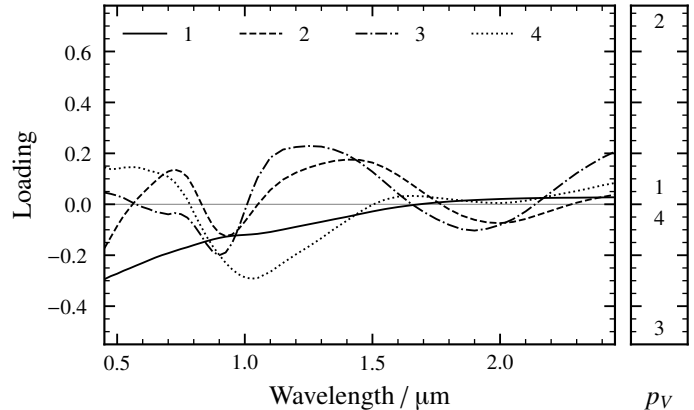


Figure 3: The four latent components of the Mixture of Common Factor Analyzers model trained on the input data. The left hand side gives the loading of the spectral data dimensions for each latent component, while the right hand side shows the loading corresponding to the albedo.

around 1 μm . Components two and three resemble the spectra of pyroxene minerals due to their bands at 1 μm and 2 μm , though the band minima and depths differ between the components. The strongest distinction between these two components is the visible slope, which is positive for component two and negative for component three. Component three has a slight absorption feature at 0.7 μm . The fourth component depicts an olivine-like 1 μm band structure. The albedo contributes marginally to the first and fourth latent component, while component two has a large positive loading and component three a large negative loading to it.

The latent scores of the asteroid observations are shown in Figs. 4 and 5. The input data depicts a larger variance when projected along the first two components rather than along the last two due to the initialisation of the latent components with PPCA. It is further intuitive that the featureless spectra will show little variance when projected along the pyroxene- and olivine-like axes z_2 , z_3 , and z_4 .

Figures 4 and 5 additionally indicate the mean latent scores of all asteroids assigned to a given asteroid class, designated by the class letter and derived in the following sections. As an example for the interpretation of latent scores, we point out here that the degeneracy between the classes E and S in the latent scores depicted in Fig. 4 is the result of the large loading of the albedo in the second component, which offsets the generally featureless E-types with respect to the feature-rich but fainter S-types. This degeneracy is resolved in other latent components, as can be seen in Fig. 5.

3.3 Clusters

Concurrent with the dimensionality reduction, the input data is divided into 50 Gaussian clusters during the model training. The clusters are not constrained in their covariances, yielding a wide range of cluster shapes and orientations in the latent space. Illustrating the distribution of the clusters in the four-dimensional latent space is not practical due to their large number, instead transformed spectra.

¹⁰Note that the latent loadings represent the variance of the In-

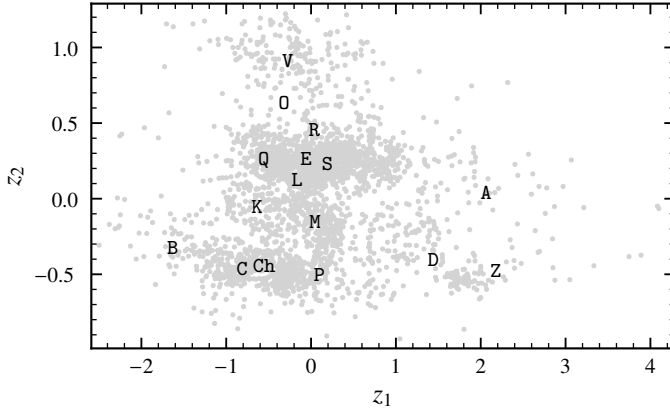


Figure 4: The latent scores of the input data projected along the first two latent components are shown as grey circles. The mean score of all asteroids assigned to a given class is indicated by the class letter. For better readability, class C has been shifted by -0.1 in z_1 .

we show the distributions of input spectra and albedos over the clusters in Figs. 6 and A.1 respectively.

Most clusters occupy a narrow volume in the latent space and encompass Gaussian populations in previously recognized classes such as S and V. When building the asteroid classes from the clustering, we map the probability of any sample to belong to either of these narrow clusters one-to-one to the respective asteroid class. As an example, for all observations, the probability to belong to cluster 0 is added to the probability p_S of belonging to the S-types, refer to Fig. 6. Additional S-like clusters such as cluster 6 further add to p_S . 33 clusters are mapped to a single asteroid class in this manner.

Other clusters either capture continuous trends between classes or the diffuse background population. An example for the former is cluster 22, containing spectra from both M- and P-types, and for the latter cluster 13, containing observations with varying spectral characteristics and albedos. For these clusters, we implement decision trees to separate the observations into mostly two or three distinct classes. These decision trees are described in Sect. 4 on a per-class basis at the end of each class description. The probability to belong to either of these clusters is split and added to the respective class probabilities following the decision trees. As an example, cluster 22 is resolved via the albedo. If no albedo is present in the observation, the cluster probability is added entirely to p_X , otherwise, it is split between p_M and p_P proportionally based on the albedo distribution of M- and P-types, derived in Sect. 3.4.2.

For clusters 13, 29, and 41, we note that they capture objects with high variability in their spectral and albedo features. These are either unique objects, such as the only O-types (3628) *Boznemcova* and (7472) *Kumakiri* in cluster 13, or spectra of questionable quality. We resolve these clusters with decision trees based on GMMs into different classes: cluster 13 into C, O, Q, cluster 41 into B and V, and cluster 29 into every class except for E, K, L, O, R, X, and Z. Objects in either of the three clusters are flagged in the classification output as DIFFUSE and should undergo visual scrutiny.

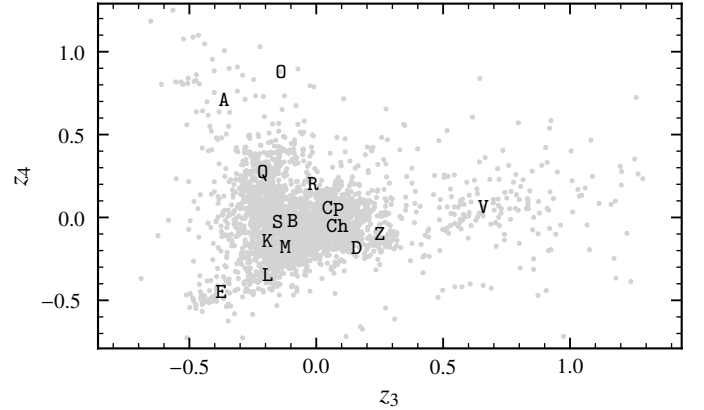


Figure 5: As Fig. 4, giving the scores in the third and fourth latent components instead. For better readability, class S has been shifted by -0.02 in z_3 and classes C and P by 0.04 in z_4 .

3.4 Classes

3.4.1 Class Continuity

When deriving the mapping of the Gaussian clusters to the asteroid classes, we strive to maximize the resemblance of the resulting taxonomy to the established system by Tholen (1984) and the Bus-DeMeo system. For any change in the classes, we weigh the evidence in the data to necessitate the change against the overall practicality of class continuity, opting for the latter when in doubt. Furthermore, we also take into account mineralogic and meteoritic interpretations established in the literature using observables outside this feature space, allowing to derive classes which are more useful for communicating class properties within the community. These influences from outside the data-driven approach are stated in the description of the respective class in Sect. 4.

The main drivers for the evolution of the class scheme are twofold; (1) the fundamental difference between the probabilistic clustering employed here and the visual clustering used in previous schemes, affecting specifically classes which reflect continuous trends in the asteroid population, and (2) the re-introduction of the albedo to the observables of the taxonomy.

The fundamental division of asteroids into feature-poor and feature-rich populations, the C- and S-complexes, is the baseline of our scheme as it has been since the first taxonomic efforts by Chapman et al. (1975). A small population of asteroids with faint features occupies the space between these complexes in DeMeo et al. (2009), separated into the classes K, L, Xc, Xe, Xk, and T. Due to the taxonomic information provided by the albedo and targeted campaigns of these populations (e.g. Ockert-Bell et al. 2010; Neeley et al. 2014), this population has grown considerably, to the point that we recognize it as a third complex which we dub the M-complex based on its most populous class.

Taxonomic constants such as the A- and V-types represent no challenge in identification. More difficult prove the definition of the Q-types, which represents a continuous trend towards smaller slopes compared to the S-types and as such does not separate clearly in the latent space. In favour of class continuity, we still identify a population in the S-complex as Q-types. Subclasses

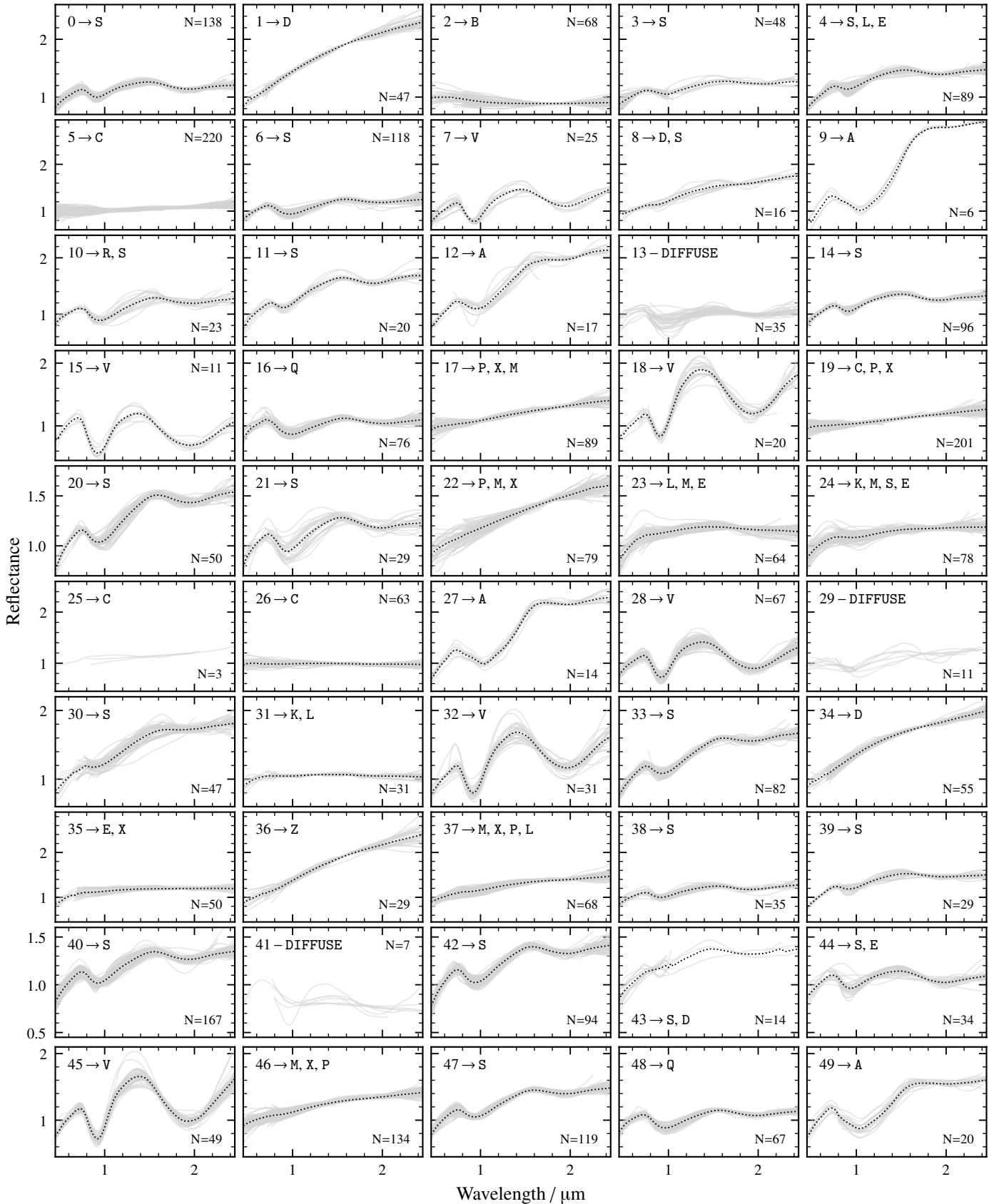


Figure 6: Overview of the asteroid spectra assigned to each cluster, including the number N of spectra and the asteroid classes to which the cluster contributes, excluding classes with fewer than 3 contributed observations except for cluster 25 which only has three members. The classes are sorted by the total number of observations the cluster contributed. The dotted line gives the mean value of the spectra per cluster except for diffuse clusters and cluster 25. The mean spectra are normalized to unity at $0.55 \mu\text{m}$. Note the change in y-axis limits per row.

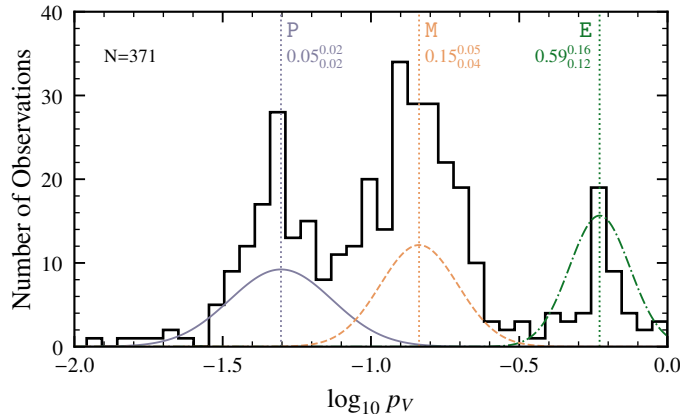


Figure 7: The spectral degeneracy of the X-complex’ is resolved by fitting a three-component Gaussian mixture model to its albedo distribution, consisting of N observations and shown in the histogram. The fitted components are given by the solid, dashed, and dash-dotted lines, scaled by a factor of 4 for readability. The vertical dotted lines give the mean values of components, labeled by the established class designations P, M, and E in order of ascending albedo. The numbers below the class labels give the mean p_V and the upper and lower 1σ -limits per class.

such as Sa, Sq, and Sr are, however, not identified, as we observe numerous clusters with varying slopes and mineralogies in the S-complex. Labeling each cluster with a secondary letter would increase the entropy of the taxonomic system and overall lead to more confusion than resolution. Furthermore, we note an overall large variability between observations of single asteroids which often exceeds the variability between these subclasses. Instead, we highlight the different mineralogical interpretations of these clusters in Sect. 4.5.1.

3.4.2 Resolving the X-Complex

Solving the spectral degeneracy of the X-complex in the Bus-DeMeo scheme is the main motivation to re-introduce the albedo to the taxonomic system. As such, the principal evolution of the taxonomy occurs for X-types. We employ the system established in Tholen (1984); asteroids in the X-complex are differentiated based on their albedo values and are labelled P, M, and E in ascending order of albedo, while the letter X is retained for observations without albedo. However, instead of applying strict limits,¹¹ we model the joint albedo distribution of all observations in clusters which we consider to be X-like based on their spectral appearance: clusters 17, 22, 35, 37, and 46. The employed model is a GMM with three components. In Fig. 7, we show the model fit to the albedo distribution of the X-complex, as well as the derived mean and standard deviations in p_V for the E-, M-, and P-class. Any asteroid which falls into one of the aforementioned clusters and has an albedo observation is assigned based on its probability in this model to the respective class. The subclassification indicating the presence of features in the spectra (e and k) is retained and discussed in the following subsection.

¹¹Tholen (1984) applied visual albedo separations of ~ 0.06 between P and M and ~ 0.28 for M and E.

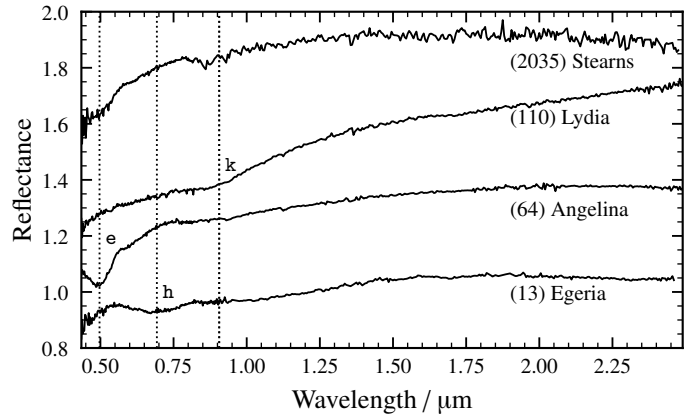


Figure 8: Shown are example spectra carrying the e-, h-, or k-feature which are recognized in this taxonomic system. The mean band centers derived from all visually-identified features in the spectral observations is indicated by the vertical dotted lines (e: $0.50\ \mu\text{m}$, h: $0.69\ \mu\text{m}$, k: $0.91\ \mu\text{m}$). (2035) *Stearns* exhibits both the e- and the k-feature. Data from SMASS.¹²

3.4.3 Feature Flags

The Bus-DeMeo system recognizes four classes which are based on the presence of distinct absorption features in addition to the overall shape of the spectra: (1) Ch, exhibiting a feature around $0.7\ \mu\text{m}$ associated to possible surface hydration (e.g. Rivkin et al. 2015), (2) Xe, showing a narrow feature at $0.5\ \mu\text{m}$ (Bus and Binzel 2002b), (3) Xk, depicting a faint, broad feature between $0.8 - 1.0\ \mu\text{m}$ (Bus and Binzel 2002b), and (4) Xn, with a feature around $0.9\ \mu\text{m}$ (Binzel et al. 2019). Example spectra carrying the e-, h-, and k-features are shown in Fig. 8.

The identification and flagging of these features by use of the secondary letters in the class designation is carried over in this scheme with a slight modification. First, we do not differentiate between the k- and the n-feature. Both are centered around $0.9\ \mu\text{m}$ and after slope removal, we find no appreciable systematic difference between the features in a sample of spectra previously classified as Xk or Xn. We do not rule out that these features are imprinted by different surface mineralogies, however, we choose the evidence in the data over class continuity, we decide to drop the n-feature and continue with only the k-feature.

Second, we do not reserve unique classes for observations depicting the e- or the k-feature. As discussed in Sect. 4.3, both features are prevalent in members of the X-complex showing a variety of spectral slopes and albedos. We judge the latter two properties to be more important when deriving classes than the presence of a single feature. Furthermore, we note that e and k are not mutually exclusive, e.g. (2035) *Stearns* depicts both features as shown in Fig. 8. We thus decide to flag the presence of these features by appending the respective letter to the class designation without considering the resulting combinations such as Mk or Eek as proper classes.

On the other hand, the h-feature is treated consistently with the Bus-DeMeo system. It is exclusive to the members of the C-complex and displays a much narrower, continuous distribution than the other two features, as shown in Sect. 4.1. Any sample depicting the $0.7\ \mu\text{m}$ band is assigned to the Ch-class, regardless

of the subclass in the C-complex that the spectra falls in.

The features are identified in a semi-automated manner. For each feature, we have defined a wavelength interval around the band center in which the spectral continuum is removed and the reflectance is fitted using a polynomial of fourth degree, following Fornasier et al. (2014). Both the interval and the band center were defined heuristically using a training sample of visually identified features and are given in Table B.1. Using the polynomial fit, we estimate the band depth with respect to the continuum, the band center, and its signal-to-noise ratio. The latter is given by the ratio of the band depth to the reflectance uncertainty, which is estimated using the residuals of the polynomial fit. The band is considered to be present if the band center is within three standard deviations of the expected position derived from the training sample and the signal-to-noise is larger than one.

The fitting procedure is run automatically to identify the h-feature in spectra classified as members of the C-complex (B, C, P, and the degenerate class X, refer to Sect. 4.1) and the e- and k-features for those belonging to the X-complex (E, M, P, and X). In practice, we find that relying on the automated band identification yields many false positives given the low threshold of one in the signal-to-noise ratio. However, increasing the required signal suppresses the detection of too many features. Hence, we recommend a semi-automated approach where the bands are fitted automatically and the observer visually confirms the quality of the fit. The fitting and confirmation are handled by the classification tool presented in Sect. 5. In the 2983 spectra classified during the clustering, 13 (144, 135) carry the e-feature (h-feature, k-feature). For 392 spectra (361, 360), no conclusion could be made as the spectral region is missing.

The k-feature is particularly challenging to observe as it falls into the transition of visible and near-infrared spectra, which are acquired using different instruments. Merging the spectral parts is a non-trivial and several subjective decisions have to be made, as outlined in Clark et al. (2009). The unknown offsets between visible and near-infrared can give rise to an artificial feature when joining the observations. In case of the e-feature, Bus and Binzel (2002a) point out a systematic feature between 0.515 μm and 0.535 μm in the SMASS spectra, which are frequently used to compliment acquired NIR-only spectra. Hence, we emphasize here that the e-feature should only be considered to be present if its band center well below this wavelength range.

3.4.4 Class Per Asteroid

549 of the 2125 asteroids in the input data have more than one sample in the input data. These observations may or may not have been assigned to the same class, opening the possibility that asteroids have different classes assigned. We resolve these ambiguities by computing the sum of the class probabilities across all observations of the asteroid, weighted by the fraction of observed data dimensions. Observations with albedo values received an additional weight corresponding to 25 data dimensions, meaning that a visible-only spectrum including albedo has approximately as much weight as a VisNIR spectrum without albedo. If either of the e-, h-, or k-feature is detected in any of the observations, the final class of the asteroid carries the respective suffix letter.

In Table 1, we report the total number of observations per taxonomic class, followed by the number of distinct asteroids in

the class. The latter number only includes asteroids which were assigned to the class after the merging procedure outlined above in the case of multiple observations.

4 DISCUSSION

In the following, we discuss the main properties of the 17 classes defined in this taxonomy in data- and latent space, structured into three complexes: C, M, and S. We motivate the class scheme and point out where it aligns with or deviates from the existing classifications, in particular the taxonomy by Tholen (1984) and the Bus-DeMeo system (Bus and Binzel 2002b; DeMeo et al. 2009), which are the closest predecessors in terms of the observables.

A general overview of the class properties in data space is given in Figs. C.2 and C.3. Table 1 gives an overview of the number of samples and asteroids per taxonomical and orbital class. Tables 2 and 3 at the end of this section show an evolution of the taxonomic scheme and describe the classes defined in this taxonomy, including an overview of the spectra of class prototype asteroids, most of which are discussed in the text. The mean spectra and albedos for each class (“class templates”) are available in the CDS repository. The X-class is not discussed separately as its members are covered by the classes E, M, and P.

4.1 C-Complex: B, C, Ch, P

The members of the C-complex are found throughout the Main Belt and dominate the regions past the 3:1 mean-motion resonance in terms of number and mass (DeMeo and Carry 2014; Vernazza et al. 2017). Their spectral appearance is generally feature-poor apart from the h-feature at 0.7 μm observed in about one third of the population and associated to phyllosilicates present on the surface (Rivkin 2012). Instead, the diversity of the complex constituents presents itself both in the slope and the shape of the spectra, the former ranging from blue over neutral to red and the latter from overall linear to a concave appearance attributed to a carbonaceous surface composition including magnetite (Chapman et al. 1975; Gaffey and McCord 1979; Cloutis et al. 1990b)

Common meteorite linkages to the population of the C-complex involve carbonaceous chondrites such as CI, CK, CM and CO with different degrees of thermal metamorphism or aqueous alteration (Hiroi et al. 1996; Clark et al. 2010; Cloutis et al. 2011; León et al. 2012). However, the paucity of these meteorite groups among the falls even after bias-correction is difficult to reconcile with the abundance of the complex members in the Main Belt, leading Vernazza et al. (2015) to suggest *Interplanetary Dust Particles* (IDPs) as analogues for the non-hydrated asteroids. Using a radiative transfer model, the spectral appearance of most C-complex asteroids is well matched using constituents of chondritic-porous IDPs. The open question on the surface composition is decisive for the behaviour of the asteroids under spectral weathering influence. Both laboratory irradiation experiments (Lantz et al. 2017, 2018) as well as statistical approaches (Thomas et al. 2021) show opposite trends for different initial surface compositions: while high-albedo material exhibits spectral reddening and surface darkening, low-albedo assemblages become bluer in their slope and brighter.

Apart from the C-types, Tholen (1984) defined three smaller classes based on the albedo and ultra-violet distributions. B represents “bright-C”-types, with visual albedos around 10 %, while F

¹²<https://smass.mit.edu>

Table 1: The distribution of observations and asteroids over the 17 classes defined in this taxonomy. The second column gives the number of observations assigned to each class, while the third and all following columns refer to the number of unique asteroids which are assigned to the class. DM09 refers to DeMeo et al. (2009). The fraction in this column does not add to 100 % due to the missing T-class in this scheme. The orbital classes use the following acronyms: NEA - Near-Earth Asteroids; MC - Mars-Crosser; H - Hungaria; IMB - Inner Main Belt; MMB - Middle Main Belt; OMB - Outer Main Belt; Trojan - Jovian Trojans.

Class	Samples	Asteroids	Fraction		Orbital Class								
			This Work	DM09	NEA	MC	H	IMB	MMB	OMB	Cybele	Hilda	Trojan
A	57	32	1.5	1.6	2	3	2	7	10	8	-	-	-
B	68	45	2.1	1.1	15	4	1	12	5	8	-	-	-
C	299	221	10.4	7.3	69	8	2	89	72	79	2	2	5
Ch	144	107	5.0	4.8	9	2	-	20	47	26	2	-	1
D	119	82	3.9	4.3	6	1	-	1	4	5	5	16	44
E	65	46	2.2	-	7	4	27	4	3	1	-	-	-
K	59	42	2.0	4.3	21	2	-	5	2	12	-	-	-
L	76	58	2.7	5.9	20	4	3	4	22	3	-	-	2
M	252	142	6.7	-	29	7	2	17	47	28	-	2	10
O	4	2	0.1	0.3	-	-	-	-	1	1	-	-	-
P	195	135	6.4	-	14	6	1	11	26	36	12	12	17
Q	158	107	5.0	2.2	89	5	-	7	4	2	-	-	-
R	15	10	0.5	0.3	7	-	-	2	-	1	-	-	-
S	1188	898	42.3	53.8	404	101	35	140	172	45	-	1	-
V	206	142	6.7	4.6	28	2	-	104	4	4	-	-	-
X	50	33	1.6	8.6	20	8	2	1	-	2	-	-	-
Z	28	23	1.1	-	1	-	1	4	6	3	-	1	7
Σ	2983	2125	100	98.9	741	157	76	428	425	264	21	34	86

and G are characterized by their behaviour in the UV wavelength region the former flat, the latter showing a strong absorption behaviour. The Bus-DeMeo system retained the classes B and C and extended the taxonomy by addition of the Ch class, designating hydrated C-type asteroids, as well as the classes Cb, Cg, and Cgh, which describe different slope behaviours in different wavelength regions. Neither system counts the P-class as member of the C- but rather as member of the X-complex.

In this taxonomy, we divide the C-complex into four classes: B, C, Ch, P. The P-class is here defined for the first time in both albedo and spectral appearance, allowing us to move it from the X-complex and firmly establish it as part of the C-complex. Any object within the complex which exhibits the h-feature is classified as a Ch-type, even if it falls into B or P. The distribution of reflectance spectra and visual albedos for each class is shown in Fig. 9. The heterogeneous yet continuous distribution of the C-complex members in latent space is illustrated in Fig. 10. As change in slope and a broad feature around $1\ \mu\text{m}$ – $1.3\ \mu\text{m}$ are the main differentiators, the complex members split best in the z_1 and z_4 latent dimensions.¹³ Note that the apparent diagonal gaps between the C- and Ch-class members in the lower part of Fig. 10 are an artifact of the spectral normalization and not of physical nature, as shown by the large number of asteroids which have samples on either side of the gaps.

4.1.1 B-Types

The B-class was first defined in Tholen (1984) based on their on average large albedo in comparison to the other members of

the C-complex. With the disappearance of the UV wavelength region from taxonomy, F-types are no longer distinguishable from B-types, and the generally high albedo distribution of the latter has become a broad distribution with a standard deviation of around 10 %, see Fig. 9. This distribution is further visible in the large variance in the z_2 -scores of B-types (Fig. 10). Instead, the “bright-C” (Tholen 1984) are best identified a by another common interpretation of the class mnemonic, their “blue” slope longward of $\sim 0.7\ \mu\text{m}$, causing a readily-apparent distinction from other classes specifically in the z_1 latent score. Nevertheless, the B-types do not separate entirely from the neighbouring C-types and form a diffuse but continuous branch of the complex, as shown in Fig. 10.

The class variance in z_1 - z_2 indicates that bluer B-types further tend to be brighter. As shown in the upper focus (a) in Fig. 10, both the archetype B-type (2) *Pallas* as well as near-Earth asteroid (3200) *Phaethon* are among the bluest and brightest class members. (531) *Zerlina* is further highlighted as member of the *Pallas* collisional family, for which Alí-Lagoa et al. (2016) note a significantly larger average albedo compared to the remaining B-types. In z_4 , B-types have larger scores than other C-complex members with z_1 -score due to the visible part of the fourth latent component resembling the B spectral region (compare Figs. 3 and 9).

45 asteroids (2.1 %) are classified as B-types in this study. The B-class is made up of a single cluster (2) and not subject to any decision tree. We note that the *Themis*-like B-types with a neutral-to-reddish slope in the NIR as described in Clark et al. (2010) and León et al. (2012) are C-types in this taxonomy, in agreement with their classification in the Bus-DeMeo system, refer to the lower focus (c) in Fig. 10.

¹³Note that we consider an absorption feature to be concave, while other works such as Lantz et al. (2018) define it as convex.

4.1.2 C-Types

The carbonaceous C-types present spectra with a neutral to small red slope and are generally featureless except for a broad feature around $1.3\ \mu\text{m}$ which may give the spectrum an overall concave shape. In the upper part of Fig. 10, we observe a uniform distribution of the C-types in z_1 - z_2 with the class variance aligned with the z_1 axis. z_2 is not a suitable projection for the C-types as they are featureless and present a narrow albedo distribution, as shown in Fig. 9. Instead, the concave feature shape is captured in z_4 , hence, in the lower part of Fig. 10, we observe a more structured clustering. The positive correlation of z_1 and z_4 scores among the C-types indicates that the spectra on average get more concave as they get redder. Nevertheless, the wide and continuous distribution around this general trend prevents us from defining analogues to the classes Cb, Cg, and Cgh in the Bus-DeMeo system as we aim to refrain from subjectively partitioning the latent space.

Both (1) *Ceres* and (10) *Hygiea* are members of the C-class, refer to the upper focus (b) in Fig. 10. In the lower focus (c), we highlight (24) *Themis*, (45) *Eugenia*, and (52) *Europa*. All these asteroids are well matched by the models composed of IDP constituents as described in (Vernazza et al. 2015) and have on average larger z_4 scores than the Ch-class members of comparable slope.

221 asteroids (10.4 %) are classified as C-types in this study. C-types are present in three different clusters (5, 19, 26, where the first two are the two largest clusters among the 50 clusters in the model). Cluster 19 contains both prominent C-types such as (45) *Eugenia* and (52) *Europa* as well as prominent P-types such as (65) *Cybele* and (87) *Sylvia*, as shown in the upper focus (c) in Fig. 10. The cluster resembles the Cb-class from the Bus-DeMeo system. We choose to split this cluster into two components (C and P) using a Gaussian mixture model in z_1 - z_4 . While we generally aimed to keep the number of decision trees post-clustering to a minimum, we make the choice here to (1) follow the mineralogical interpretation of the C-complex given e.g. in Vernazza et al. (2015) and Marsset et al. (2016) as well as (2) increase class continuity for the objects in these clusters.

4.1.3 Ch-Types

Unlike for the other feature flags outlined in Sect. 3.4.3 we reserve a unique class for the $0.7\ \mu\text{m}$ h-feature, following the convention of the Bus-DeMeo system. We observe the continuous and narrow distribution of samples carrying this feature akin to the other classes in the C-complex. Furthermore, as above for the C-types, we recognize the mineralogical and meteoritic interpretation of the C-complex members in the literature (e.g. Cloutis et al. 2011; Vernazza et al. 2015; Marsset et al. 2016)

While degenerate with the distribution of C-types in z_1 - z_2 , the Ch-types have generally lower scores in z_4 than the C-types, corresponding to linear rather than concave spectra. In the lower foci (b) and (d) of Fig. 10, we highlight asteroids (41) *Daphne*, (49) *Pales*, (121) *Hermione* (144) *Vibilia*, and (159) *Aemilia*, all of which are compatible with CM chondrites spectra following the interpretation in Vernazza et al. (2015). (130) *Elektra* is further linked to these objects based on the density measurements (Carr 2012; Yang et al. 2016; Hanuš et al. 2017).

The $0.7\ \mu\text{m}$ h-feature has been observed in at least one observa-

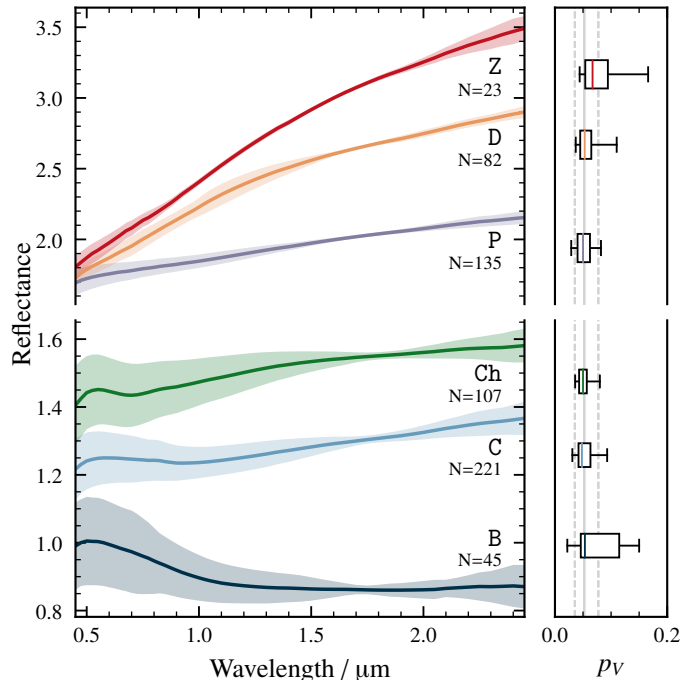


Figure 9: Depicted are the mean (solid line) and standard deviation (shaded area) of the reflectance spectra for each class and endmember of the C-complex on the left hand side. Note the change in the reflectance scale between B, C, Ch and P, D, Z. The number N of unique asteroids assigned to each class is given below the class letter. On the right hand side, we give the median (solid line), the lower and upper quartiles (box), and the 5 and 95 percentiles of the distribution of visual albedos within the class. The vertical gray lines give the mean albedo (solid) and the upper and lower standard deviation (dashed) within the whole complex. These latter values are $0.05^{+0.03}_{-0.02}$ for the C-complex.

tion of 107 asteroids (5.0 %). Members of the Ch-class are found in clusters 2, 5, 17, 19, and 26. The assignment requires the identification of the $0.7\ \mu\text{m}$ h-feature. Within the C-complex only, 20.4 % of samples present the h-feature. The actual number is likely higher as 12.1 % of samples in the C-complex are missing the visible wavelength range, e.g. a NIR-only spectrum of (41) *Daphne* indicated as C-type in the lower focus (b) of Fig. 10.

4.1.4 P-Types

The P-types have been absent from the taxonomic schemes since Bus and Binzel (2002b) and as such, no definition of the Vis-NIR behaviour exists. As part of the X-complex, the “pseudo-M” (Gradie and Tedesco 1982) types are spectrally degenerate to the E- and M-types in the visible wavelength range, specifically, the ECAS colours. In the NIR, P-types show a red, linear slope, refer to Fig. 9. We find that the spectral degeneracy between P and M continues in the NIR, while E-types differentiate by showing overall neutral slope. P and M have to be distinguished by visual albedo observations, which is about 5 % for P-types.

As the X-complex is dissolved in this taxonomy, we assign the class to the C-complex following the proximity to the other classes in Fig. 10. This assignment is further in line with the IDP interpretation (Vernazza et al. 2015; Marsset et al. 2016). In z_1 - z_4 -space,

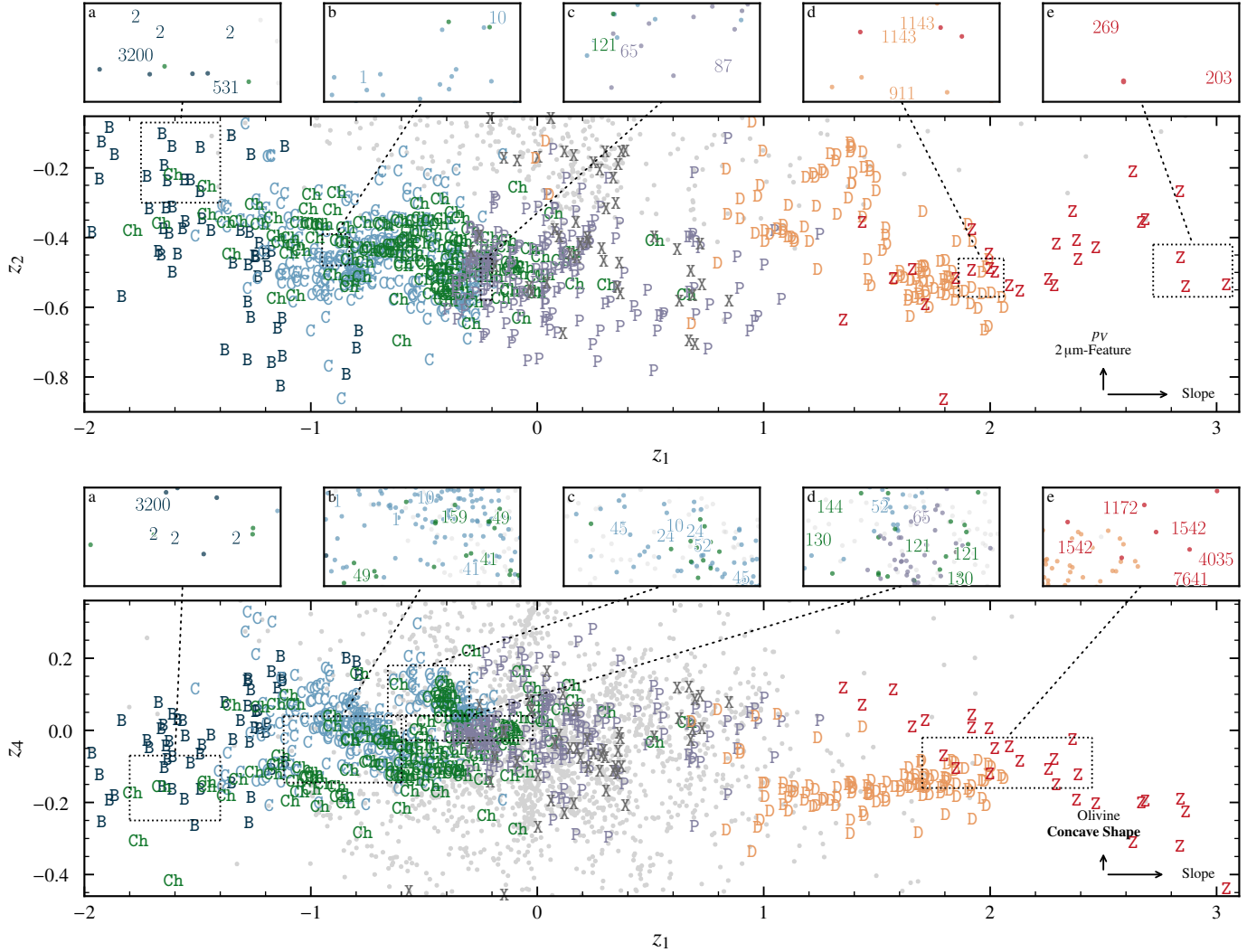


Figure 10: The distribution of the C-complex and its endmember classes D and Z in the first latent component versus the second (top) and the fourth (bottom). The samples assigned to each class are given with the respective class letter. The latent scores of all samples outside these classes are shown as gray circles. Some outliers in z_2 and z_4 are not shown for readability. The five smaller figures above the larger ones show regions-of-interest, where a selection of asteroids is highlighted by replacing the symbol by the respective asteroid’s number.

we observe a high-density cluster of P-types immediately adjacent to C-types. These samples are spectrally similar to the Cb-class in the Bus-DeMeo system. There further is a more diffuse population of P-types building a bridge between the C-complex and the D-class.

The P-class is part both of the former X-complex and the new C-complex. Observations assigned to the P-class are thus inspected for all three features. While 19.2% of samples in the P-class present the h-feature, we note that no sample carries the k-feature, which is most prominent in the M-class. Three samples assigned to P show the e-feature, yet they belong to asteroids which are later assigned to the M-class ((4660) *Nereus* and (5645) *1990 SP*). The k-feature may thus be a reliable differentiator between the spectrally degenerate M and P. The distribution of these features is further discussed in Sect. 4.3.

135 asteroids (6.4%) are classified as P-types in this study. P

is built primarily from clusters 17, 19, and 22, where the second one entails the continuous transition to class C and the first and third M-types. As mentioned above, we used the prototypes (65) *Cybele* and (87) *Sylvia* to differentiate between the classes, though assigning both to the C-types would have been justified as well given the cluster trend depicted in Fig. 10, refer to the upper focus (c).

4.2 Endmembers: D, Z

We refer to D and Z as endmembers due to the visible gap between their members and the C-complex in the latent space in Fig. 10, however, a part of the P-types forms a bridge population between both.

4.2.1 D-Types

The defining property of dark D-type asteroids is their featureless and strongly red-sloped spectrum both in the visible as well as in the NIR (Tholen 1984; DeMeo et al. 2009). They are predominantly found beyond the outer main belt, especially among the Jupiter Trojan population, where they dominate the region in terms of mass (DeMeo and Carry 2013, 2014).

D-types form a homogeneous population both in spectral- and albedo space, as shown in Fig. 9. This homogeneity is mirrored in the latent scores z_1 and z_4 as well, refer to Fig. 10, where in the upper focus(d) we show the positions of (911) *Agamemnon* and (1143) *Odysseus*. In the second latent score, the D-types appear to split into a blue and a red population. We attribute this again to the normalization of the spectra, which can cause these spurious offsets. Comparing the samples in the clusters showed no significant different in the observables, and both (2246) *Bowell* as well as (2674) *Pandarus* are present in both clusters. Nevertheless, this serves as example that the normalization algorithm we devised for the partial observations may require further improvement. Furthermore, all clusters in latent space have to be verified by comparing the members in the observed features.

82 asteroids (3.9 %) are classified as D-types in this study. D-types appear predominantly in two clusters, the homogeneous main cluster 1 and a more diffuse cluster 34 which may contain interlopers of classes P and M. Furthermore, there are two small clusters containing both D- and S-types. Cluster 8 has 16 VisNIR spectra of D-types and strongly-sloped S-types, which are separated using a two-component GMM in z_2 - z_4 , where the features-rich S-types have larger scores in z_2 . Cluster 43 contains 14 spectra which are mainly visible-only S-types but include 5 visible-only D-type, which we separate in the same way as in cluster 8.

4.2.2 Z-Types

The clustering revealed a low-number, diffuse cluster of featureless, extremely red objects, showing larger slopes than the D-types. Figure 10 shows that in z_1 , these objects form a continuum with the D-types, however, the classes show different variances in the z_1 - z_4 space: unlike D-types, Z-types show a clear trend towards a more convex shape with increasing slope. In addition, the classes show distinct orbital distributions, as illustrated in Fig. 11. While D-types are mostly situated among the Jupiter Trojan population and the Hildas, these extremely red objects are largely scattered over the Main Belt. Three members of this population ((3283) *Skorina*, (15112) *Arlenewolfe*, and (17906) 1999 *FG32*) have previously been recognized in SDSS observations (e.g. Carvano et al. 2010) and described in a follow-up study by DeMeo et al. (2014), who further identified (908) *Buda* as similar object.

The distinct distributions both in latent as well as in orbital space prompt us to define a new class for this group of minor bodies. We propose the letter Z, which has previously been suggested by Mueller et al. (1992) for the extremely red Centaur (5145) *Pholus*. The 23 asteroids in the Z-class show overall low albedos though we note the presence of outliers in Fig. 9.

The two reddest objects in this novel class, (203) *Pompeja* and (269) *Justitia*, have been proposed to be implanted trans-Neptunian objects by Hasegawa et al. (2021). The authors suggest that complex organics material on the surface of these objects leads to the extremely red appearance. The prevalence of Z-types on the inner

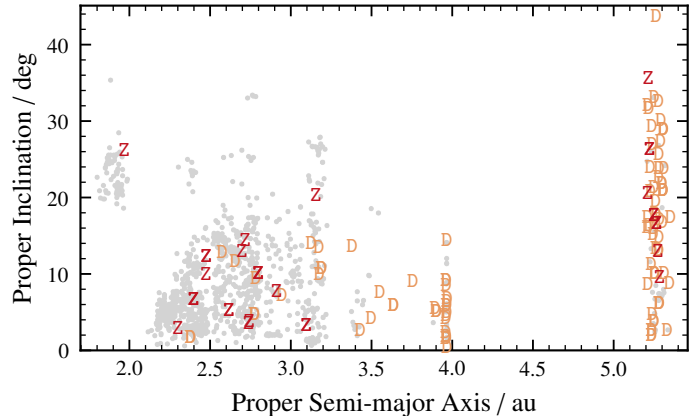


Figure 11: The orbital distribution of D- and Z-types is given by the respective class letters. The gray dots show the orbital elements of all other asteroids in the input data.

and middle Main Belt orbits of the objects could also indicate a surface process such as spectral weathering to be responsible.

23 asteroids (1.1 %) are classified as Z-types in this study. They fall exclusively into cluster 36. Yet, we expect a certain number of D-type interlopers in this class as we observe an overlap in the latent space, refer to Fig. 10 and the lower focus (e), where we have highlighted the Trojan asteroids (1172) *Aneas*, (1542) *Schalen*, (4035) *Thestor*, and (7641) *Cteatus*, which spectrally match D-types.

4.3 M-Complex: K, L, M

The M-complex comprises classes which fall both spectrally and in terms of albedo between the C- and the S-complex. Compositionally, it is the most diverse complex: while for C and S the ensemble properties can be regarded as carbonaceous, primitive for the former and siliceous, in part thermally-metamorphosed for the latter (Cloutis et al. 1990a; Cloutis et al. 2011; Vernazza et al. 2014), the likely mineralogic properties of any M-complex member cannot be given based solely on its complex membership. Meteorite analogues range from most carbonaceous chondrite clans in the meteorite collection to stony-iron and iron-meteorites (Sunshine et al. 2008; Clark et al. 2009; Ockert-Bell et al. 2010; Shepard et al. 2010; Eschrig et al. 2021) Indeed, the only unifying property of these objects appear to be the spectral appearance with absent or generally faint features around 0.9 μm or 1.9 μm and an albedo around 15 % with the exception of the endmember class E.

Devising the cluster-to-class decision tree proved challenging in this complex. In combination with the faint features, we observe slight variations in the slope in the NIR and class degeneracies appear when the visible information is missing. Furthermore, we cannot rely as much on previously established terminology as this is a novel complex in terms of taxonomic systems, replacing the X-complex as third complex in previous taxonomic systems. Both the K- and the L-types are more recent than the Tholen (1984) taxonomy which introduced the X-complex (Bell 1988; Bus and Binzel 2002b). The Bus-DeMeo system captures the diversity in the NIR in part in form of the X- and Xk classes, however, no clear separation between the X- and the C-complex is achieved

due to lack of the albedo information.

We split the complex into the three classes K, L, and M, shown in Fig. 12. The latter class in particular contains a wide distribution of spectral appearances and likely mineralogic compositions. Nevertheless, we opt against a division of this class as no clear separation presents itself in this study, and we advocate for a division based on observables not included in this taxonomy. The T-class which was tentatively introduced by Tholen (1984) and carried over in the Bus-DeMeo taxonomy is dropped as prototypes (114) *Kassandra* and (308) *Polyxo* are well described by the classes P and M.

4.3.1 K-Types

Members of the K-class exhibit a red slope in the visible region with a 1 μm -band associated to forsteritic olivine (Mothé-Diniz et al. 2008) and a neutral slope in the NIR. They have small z_1 - and large z_4 -scores in comparison with the complex companion classes, refer to Figs. 12 and 13. Most K-types have visual albedos between 10%–15%, a narrow distribution which is comparable to the M-types and slightly lower than the L-types.

Dynamically, most Main Belt K-types are associated to the *Eos*-family and depict on average a deeper 1 μm -band than K-types outside the family based on the z_4 -score (Clark et al. 2009), compare e.g. (402) *Chloe* and (1545) *Therhoe* to (221) *Eos* and (661) *Cloelia* in the lower focus (c) in Fig. 13.

The class-averaged slope is neutral to slightly red in the NIR. However, some members including the class archetype (221) *Eos* as well as (3028) *Zhangguoxi* have a blue NIR slope, indicated by their low z_1 scores in the upper foci (a) and (b) of Fig. 13. As the NIR spectrum is featureless above $\sim 1 \mu\text{m}$, this leads to a spectral degeneracy with the B-types, and the brighter part of the B-population requires the visible wavelength range information to be separated from the K-class. In the upper focus (a) of Fig. 13, we see that (2100) *Ra-Shalom* is classified as K-type based on two NIR spectra. The only VisNIR sample of (2100) *Ra-Shalom* in this study is classified as B-type. Note that (2100) *Ra-Shalom* is classified both as B as well as K in the literature based on its VisNIR spectrum (B: León et al. (2012) and Binzel et al. (2019), K: Shepard et al. (2008)). The same degeneracy has been reported for B and K types in for NIR spectra in (Clark et al. 2009) and in the colour-space of the VISTA MOVIS survey (Popescu et al. 2018).

The distribution in z_1 - z_2 shows a considerable overlap between M and K, with a slight gap between the populations around $z_1 = 0.3$. We considered whether the more reddish K-types may be Mk instead, however, among them are *Eos*-family members such as (579) *Sidonia* and (653) *Berenike*, as such, we consider this slope variability to be to be to K-types. The overlap is further resolved in z_3 - z_4 , where the K-class forms a denser population than the sparsely-distributed Mk-types (not shown).

42 asteroids (2.0%) are classified as K-types in this study. K-types are found in two clusters, neither of which they populate entirely on their own. Cluster 24 is shared with M-types with neutral NIR slopes, while cluster 31 contains NIR-only observations of B-types as well as L-types. We resolve the former cluster into K- and M-types using a two-component Gaussian mixture model fit to the cluster distribution in z_2 - z_3 , where K-types separate due to the large 1 μm band. Cluster 31 is only split into K and L members, as the degeneracy with NIR observations of B cannot be resolved

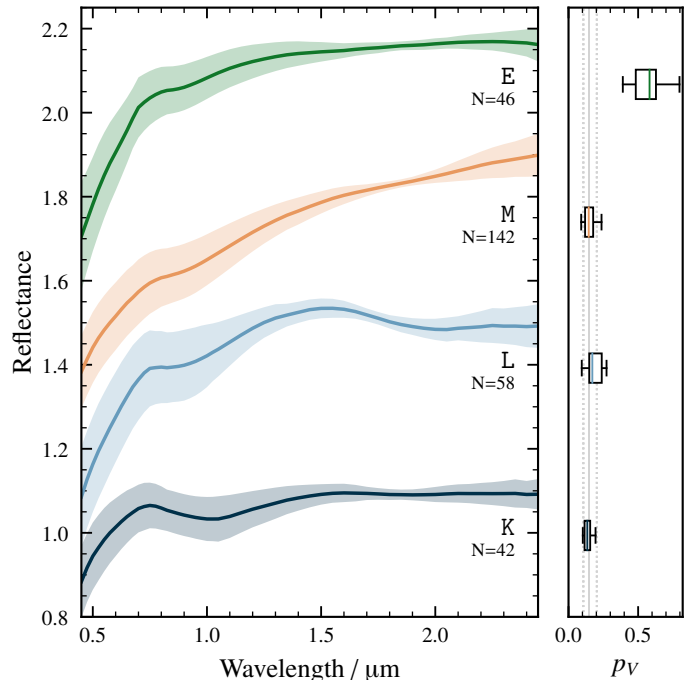


Figure 12: As Fig. 9, giving the data space properties of the M-complex. The E-class was excluded in the computation of the albedo distribution of the complex, indicated by the dotted linestyle of the upper and lower standard deviation. The albedo distribution of the M-complex excluding the E-types is $0.15^{+0.06}_{-0.04}$.

with the observables in this taxonomy. The cluster members are assigned based on their probability to belong to cluster 23 (L) or 24 (K) in z_2 - z_3 .

4.3.2 L-Types

L-type asteroids are associated to large abundances of spinel-bearing calcium-aluminium-rich inclusions due to a wide absorption feature around 2 μm (Sunshine et al. 2008). This composition would imply that the L-type parent bodies were among the first planetesimals to form in the accretion disk, making them of high interest for formation scenario studies (Devogèle et al. 2018). Yet, besides the 2 μm feature, L-types are spectrally heterogeneous in slope and shape of the visible and 1 μm -region as well as in their albedo distribution, shown in Fig. 12. The diversity of L-types makes it difficult to reliably identify them in a taxonomy based on spectral features and opens up degeneracies with a handful of neighbouring classes, such as K, M, and S.

We find that many previously classified L-types cluster in dimensions z_2 - z_4 , where they branch off of the M-complex below the S-complex together with the E-types, refer to Fig. 13. The second latent component matches the spinel-associated 2 μm -band best, giving L-types larger z_2 -scores compared to the other classes in complex, while compared to the S-types, the 0.9 μm -contribution to the z_4 score is missing.

In Fig. 13, we see that the L-types identified in z_2 - z_4 exhibit a bimodality in terms of their slope in z_1 , further shown in spectral domain in Fig. C.2. This dichotomy is not caused by the normalization of the spectra. Instead, we find that previously

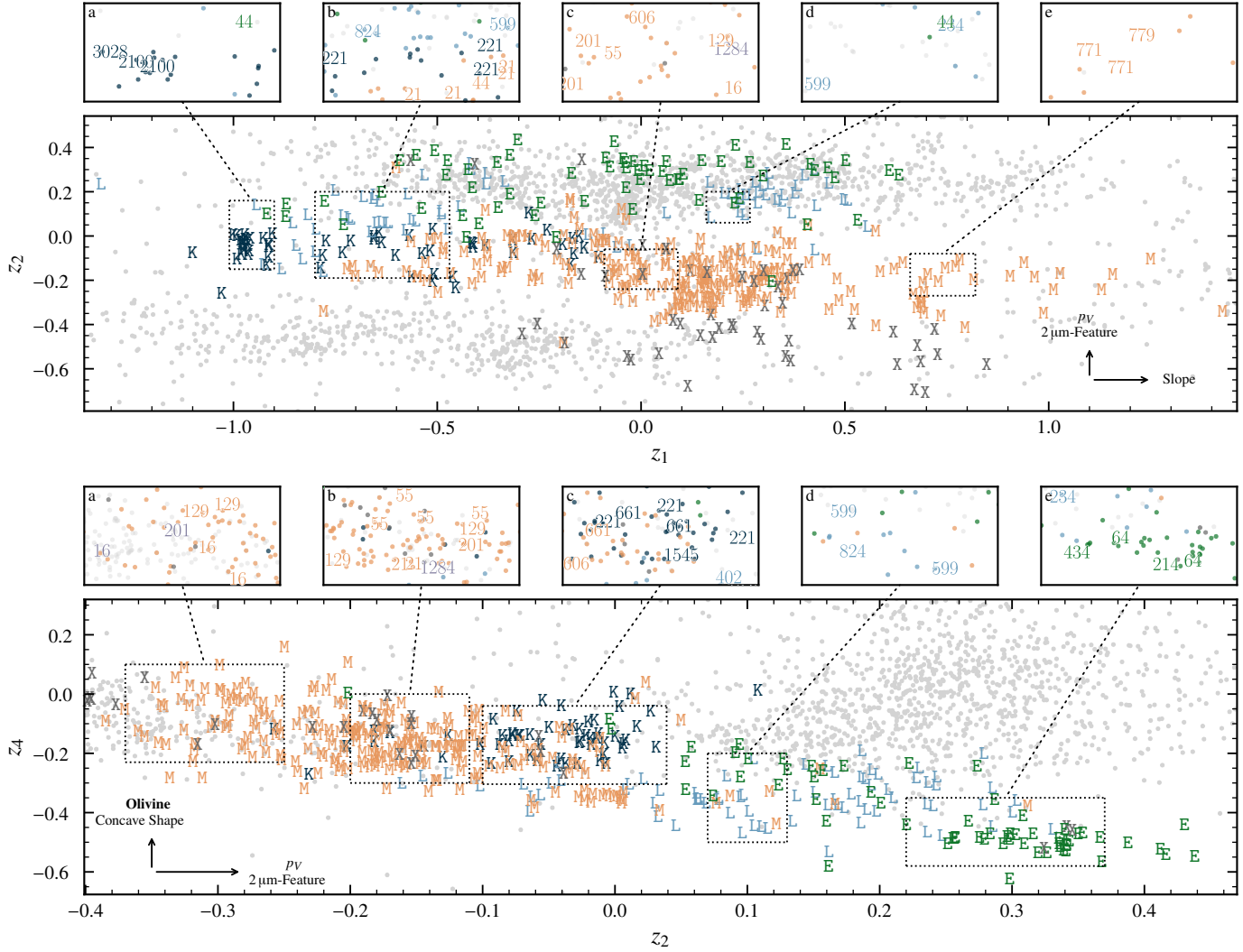


Figure 13: As Fig. 10, giving the member classes of the M-complex and its endmember class, the E-types.

classified L-types with intermediate slope such as (606) *Brangane* are classified either as M or S as they lack the 2.0 μm-feature, refer to upper focus (c) and lower focus (c) in Fig. 13. We regard the slope variability of L-types classified here as intrinsic to the class, supported by (599) *Luisa*, which has both a blue and a red spectrum, refer to the upper foci (b) and (d) and the lower focus (d) in Fig. 13.

Of particular interest among the L-types are further the subgroup referred to as Barbarians after (234) *Barbara*, which show anomalously high inversion-angles in their negative polarization branch (Cellino et al. 2014; Devogèle et al. 2018). We find that this group of asteroids has a large variance in latent space. In z_1 - z_2 , Barbarians such as (234) *Barbara*, (824) *Anastasia*, (599) *Luisa*, (606) *Brangane*, (1284) *Latvia* (the latter two are classified as M) are found in both the M- and S-complexes and at the transition region, refer to the upper foci (b) to (d) and the lower foci (b) to (e) in Fig. 13. We do not find a reliable clustering in the remaining latent scores either. The spectral L-types do not include all Barbarians, among which we observe too large diversity to derive a unique class in this taxonomy. Of the 16 Barbarians from Devogèle et al. (2018), 7 are L- and 5 are M-types. An extension

of the taxonomy observables with polarimetric observations is required to reliably identify Barbarians.

58 asteroids (2.7%) are classified as L-types in this study. L-types occur predominantly in clusters 4 and 23. As for the K-class, both clusters are populated by members from other classes as well. For cluster 4, we split L- and S-types based on a two-component Gaussian mixture model in z_3 - z_4 trained on the distribution of the members of cluster 23 and cluster 40 in this space. For cluster 23, we split L- and M-types based on a two-component Gaussian mixture model in z_1 - z_4 .

4.3.3 M-Types

The M-class is among the oldest asteroid designations (Zellner and Gradie 1976). Originally introduced to describe asteroids representing presumably metallic cores of disrupted planetesimals (Gaffey and McCord 1979; Bell et al. 1989), dedicated observational efforts have revealed a variety of objects based on their densities (Carry 2012; Vernazza et al. 2021), hydration (Rivkin 1995, 2000), radar-albedos (Shepard et al. 2010, 2015), and silicate spectral features (Clark et al. 2004; Ockert-Bell et al. 2010;

Neeley et al. 2014; Fornasier et al. 2010).

In spectral space, M-types asteroids are red with either linear or convex shapes, as shown in Fig. 12. The convex trend may even result in an overall blue slope longward of $1.5\ \mu\text{m}$, as is the case for (21) *Lutetia* in four out of five observations in this study. M-types in the lower z_1 region around (21) *Lutetia*, highlighted in the upper and lower foci (b) in Fig. 13, closely resemble the Xc-class in the Bus-DeMeo system. On the other end of the class in z_1 , asteroids like (771) *Libera* and (779) *Nina* are examples of red, linear slopes in the NIR, pointed out in the upper focus (e) in Fig. 13. M-types have an albedo distribution of 10%–20%. We note that 55 Pandora has albedo of 0.34, and one of its samples is classified as E, visible in the upper part of Fig. 13, around (0.3, -0.2).

Silicate features at $0.9\ \mu\text{m}$ or $1.9\ \mu\text{m}$ are likely more common than an entirely featureless spectrum among M-types, with 40.9% of M-type samples exhibiting the k-feature. 30.2% of the samples lack the corresponding wavelength region observed. In Fig. 14, we display the first two latent scores of samples with the e- and k-feature. The latter feature is ubiquitous among M-types, and a concentration in latent space around (16) *Psyche* is visible. (55) *Pandora*, (129) *Antigone*, and (201) *Penelope* further show the k-feature in one or several samples and are highlighted in the upper focus (c) and the lower foci (a) and (b) in Figure 13. The bands are linked to different pyroxenes (Hardersen et al. 2005), and the presence of the $1.9\ \mu\text{m}$ -band is accompanied by the $0.9\ \mu\text{m}$ band but not vice versa (Shepard et al. 2015).

The distribution of M-types in latent space and the results acquired in the studies cited above suggest that there are at least two populations of M-types, the chondritic ones, of which (21) *Lutetia* may be the archetype, as well as the metallic ones, with (16) *Psyche* as prototype (Vernazza et al. 2011; Viikinkoski et al. 2017). We see this as reasonable division of the M-class to further dissolve the compositional degeneracy of the X-complex. However, this division cannot be done based on spectra alone. To not increase the entropy of the taxonomy in a false direction, we refrain here from dividing the M-class.

142 asteroids (6.7%) are classified as M-types in this study. The main clusters containing M-types are cluster 22, 37, and 46. Smaller contributors are cluster 17 and 35. All these clusters make up the X-complex in this taxonomy and the spectra are split into E, M, and P as described in Sect. 3.4.2. Further members of the M-class are found in clusters 23 and 24, which are spectrally close to L- and K-types.

4.4 Endmembers: E-Types

E-type asteroids are linked to the enstatite achondrites (Gaffey et al. 1992). Their standout feature is a visual albedo generally above 50%, see Fig. 12. This unique property makes them easy to recognize in the reduced latent space, where they exhibit large absolute values in z_2 and z_3 , refer to Fig. 13.

Spectrally, E-types have a steep visible slope before flattening out in the NIR. In case where the albedo observation is missing, E-types are degenerate with all classes of the M-complex. As an example, we observe samples of (44) *Nysa* located in the upper foci (a) and (d), around the K- and the L-types, correctly identified as E-type due to the albedo observation. However, the third sample in the upper focus (b) lacks an associated albedo

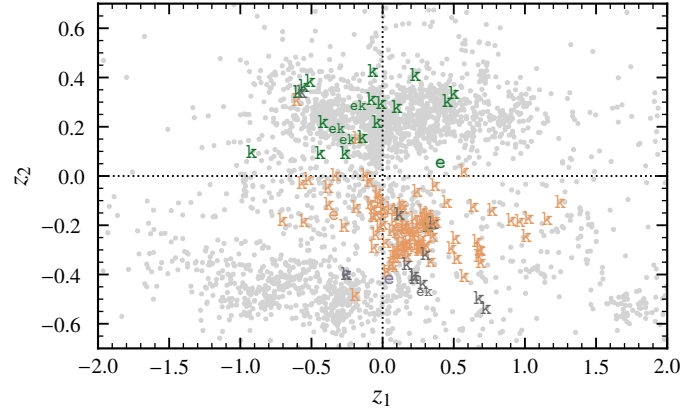


Figure 14: Distribution of observations which carry the e- and k-feature in the first two latent scores, colour-coded by the class they are assigned to: green - E, orange - M, purple - P, dimgray - X. A smaller font size is used if the observation carries both e and k.

value and is classified as an M-type. As for L and M, we notice a large intrinsic variability of the samples of unique asteroids in the E-class.

Most E-types in Tholen (1984) are classified as Xe in the Bus-DeMeo system due to the presence of the e-feature at $0.5\ \mu\text{m}$. In Fig. 14, we see that the e-feature is overall sparse compared to the k-feature. 13 samples in the M-complex exhibit the feature, while 65.4% of samples lack the corresponding wavelength region observed. Of the 13 samples, 4 are classified as E-type. Considering the relative sizes of the M- and E-class, the latter are hence more likely to exhibit the feature. We do not observe a clustering of the e-feature.

The bias towards E over M for e-feature presence may be of observational nature. As an abundance of metal on the surface of M-types may lead to a drop-off of the spectral reflectance in the ultraviolet, the $0.5\ \mu\text{m}$ -feature might not be observed as the reflectance does not increase again towards smaller wavelengths. The band is associated both to the sulfide mineral oldhamite present in aubrites (Watters and Prinz 1979), or to titanium-bearing pyroxene (Shestopalov et al. 2010). The prototype for this feature is (64) *Angelina*, while the E-class archetype (434) *Hungaria* does not present it. The k-feature is present in 30.8% of E-type samples, while 36.9% of samples lack the corresponding wavelength region observed.

(214) *Aschera* highlights the benefit of resurrecting the visual albedo: since its classification as E-type in Tholen and Barucci (1989), it has been classified as X, B, Cgh, and C in different works (Lazzaro et al. 2004; DeMeo et al. 2009; León et al. 2012). With a visual albedo above 50%, (214) *Aschera* is here classified as Ek-type and concludes its spin through the proverbial alphabet soup. Observations of (64) *Angelina*, (214) *Aschera*, and (434) *Hungaria* are highlighted in the lower focus (e) of Fig. 13.

46 asteroids (2.2%) are classified as E-types in this study. They are predominantly located in cluster 35, though other clusters of the M-complex may also contain single samples of E-types. These are identified and assigned to the E-class in a late branch of the decision tree using the albedo distributions of E, M, and P given in

Fig. 7. E-types further appear in cluster 44 among S-types, where they are identified based on a two-component GMM fitted to the albedo distribution of the cluster.

4.5 S-Complex: S, Q

The S-complex is by far the largest complex in terms of unique asteroids in this work as well as in previous taxonomies. This can be attributed to observational biases such as the numeric dominance of the S-types in the inner Main Belt and near-Earth space (DeMeo and Carry 2013, 2014; Binzel et al. 2019) and the high average albedo of more than 20%.

The abundance of S-types makes their homogeneity both in spectra and albedos as shown in Fig. 15 even more remarkable. While trends in the slope and the silicate features at 0.9 μm , 1.0 μm , and 1.9 μm are observable, these are primarily continuous trends and well explained by variations in the mineral composition, in particular olivine and pyroxene, as well as trends of thermal alteration in ordinary chondrites (Vernazza et al. (2014), Eschrig et al., submitted). S-types are one of two classes of asteroids to have an established meteorite analogue as they were linked to ordinary chondrites by the JAXA Hayabusa mission (Nakamura et al. 2011). This linkage in combination with the wealth of data on ordinary chondrites and S-types gives a solid understanding for the spectral weathering processes occurring on the surfaces of the minor bodies (Brunetto and Strazzulla 2005; Thomas et al. 2012; Chrbolková et al. 2021), which, unlike to the C-complex members, shows a universal trend of surface darkening and spectral reddening with the surface age.

We divide the S-complex into two classes: S and Q. Including the endmember classes A, R, and V, we establish all classes defined in the Tholen (1984) system while extending it with the O-class. Compared to the Bus-DeMeo system, we are reducing the taxonomy by subclasses of the S-class, as we motivate in the following.

4.5.1 S-Types

While the C has been split into subclasses since early taxonomic efforts (Gradie and Tedesco 1982; Tholen 1984), the S-class was not divided until Bus and Binzel (2002b) as the siliceous surfaces are particularly subject to changes in slope and band structure induced by phase-angle effects (Sanchez et al. 2012) as well as space weathering (Strazzulla et al. 2005).

The Bus-DeMeo system accounts for these effects by subtracting the spectral slope before classification, however, as outlined in previous sections, the partial observations prevent us from applying the method this taxonomy. Instead, we rely on the interpretation of the latent components to serve as vectors in the compositional analysis of the S-types, while detailed compositional analysis should rely on in-depth band analysis and spectral modelling.

As S-types make up the largest fraction of the input data, the latent components are trained most on the variations within this class. The second and third component both resemble pyroxene as this mineral dominates the S-class, in addition to the large contribution in terms of variance provided by the V-types. The first component resembles the slope, hence, we can approximate the vector of space weathering within the S-complex with it (e.g. Brunetto et al. 2006). S-types denoted with the w-suffix for

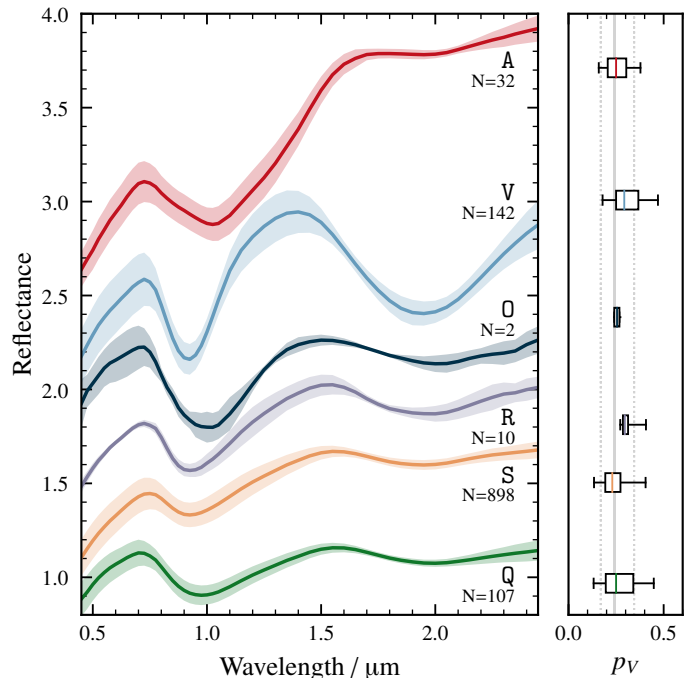


Figure 15: As Fig. 9, giving the data space properties of the S-complex. The albedo distribution of the S-complex is $0.24^{+0.10}_{-0.07}$.

“weathered” in the Bus-DeMeo system exhibit larger z_1 -scores than their class siblings with fresh surfaces. The degeneracy between a weathered S-type and an olivine-rich S-types (Sa in the Bus-DeMeo system) which is redder by mineralogy rather than by surface alteration is resolved in the third and fourth latent component, which separates the pyroxene-olivine composition of objects.

As practical example, in the upper focus (d) in Fig. 16 we show the Bus-DeMeo Sa-types (984) *Gretia* and (5131) *1990 BG* as well as the Sw-types (1019) *Strackea* and (4713) *Steel*. The lower focus (c) shows that both Sw-types have below average olivine components, indicating that the red surface is indeed due to weathering. Further shown in the focus is S-type (1036) *Ganymed*. (984) *Gretia* is classified as A-type in this study due to its large z_4 -score, refer to lower focus (a) in Fig. 16.

The Bus-DeMeo system further recognizes Sq-, Sr-, and Sv-types besides the regular S-types. The prototypes given in DeMeo et al. (2009) for these subclasses are highlighted respectively in the lower foci (b) ((3) *Juno*, (11) *Parthenope*, (43) *Ariadne*), (d) ((237) *Coelestina*, (808) *Merxia*, (1228) *Scabiosa*), and (e) ((2965) *Surikov*, (4451) *Grieve*) in Fig. 16. The continuous distribution between the main S-complex and the subclasses confirms our decision to not subdivide the S-class.

898 asteroids (42.3%) are classified as S-types in this study. The class is made up of several clusters: 0, 3, 6, 11, 14, 20, 21, 30, 33, 38, 39, 40, 42, and 47. Clusters 4, 8, 10, 43, and 44 contain members from other classes which we divide via Gaussian mixture models, as described in the respective class descriptions (L, D, R, D, and E, in order of the clusters).

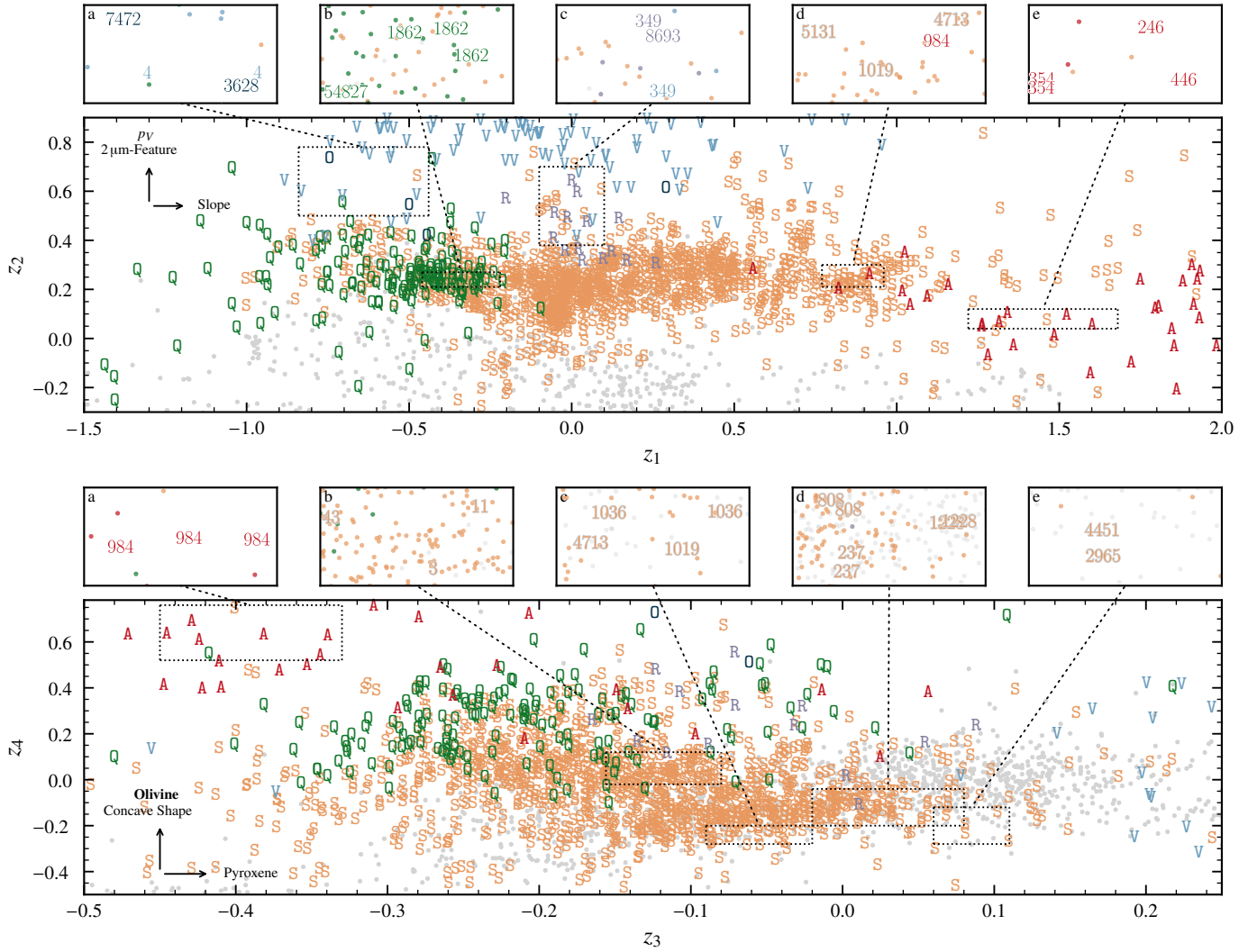


Figure 16: As Fig. 10, giving the member classes of the S-complex. For increased resolution of the S-class, the A- and V-class are only shown partially.

4.5.2 Q-Types

Q-type asteroids are mostly found in the near-Earth asteroid population and resemble spectrally the ordinary chondrites in the meteorite collection (Binzel et al. 2004). Compared to S-types, Q-types have a wider $1\ \mu\text{m}$ -band and a neutral to blue slope over the whole spectral range, refer to Fig. 15. The albedo distribution is more extended towards larger albedo values, with values of 20%–35%, in agreement with space weathering models predicting darkening of siliceous asteroids with increasing surface age (Brunetto et al. 2006).

In latent space, Q-types occupy the blue end of the S-complex in z_1 . They further separate from less-weathered S-types in the z_2 - z_3 space based on their large z_3 -scores due to the wide $1\ \mu\text{m}$ band. The archetype (1862) *Apollo* and class member (54827) *Kurpfalz* are highlighted in the upper focus (b) in Fig. 16.

107 asteroids (5.0%) are classified as Q-types in this study, 83.2% of which are near-Earth asteroids, which is considerably higher than the average of 34.4% over all asteroids in the input data. They populate clusters 16 and 48 as well as the diffuse cluster

13, further outline in Sect. 4.6.3. We considered merging the Q-class into the S-class as it represents the overall continuity in the S-complex. As for the Z-class, however, the orbital distribution of the Q-types convinced us to keep this class.

4.6 Endmembers: A, O, R, V

The endmembers of the S-complex are the well-established classes A and V as well as two classes which were initially built around single objects, O and R. Their distribution in the third and fourth latent scores is given in Fig. 17.

4.6.1 A-Types

A-type asteroids are differentiated asteroids linked to brachinite achondrites (Cruikshank and Hartmann 1984; Burbine et al. 2002; DeMeo et al. 2019) and easily recognized in spectral space by their strong red slope and deep olivine-imprint at $1\ \mu\text{m}$, refer to Fig. 15. The albedo is within the complex average of about 20%–30%.

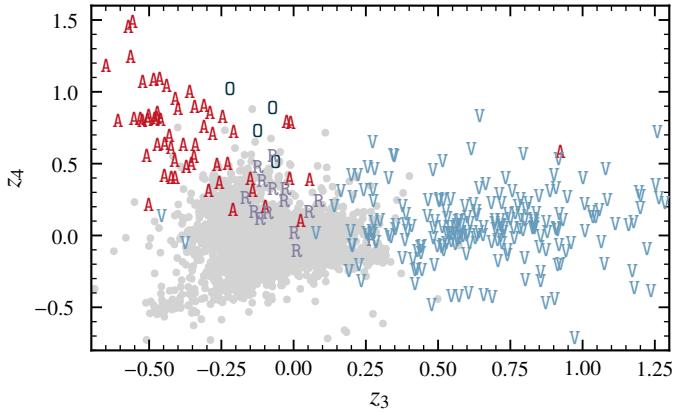


Figure 17: Distribution of the S-complex endmember classes A, O, R, and V in the last two components of the latent space.

In latent space, the red colour of A-types leads to a large score in z_1 , forming a diffuse branch off the S-type population. We highlight the prototypes (246) *Asporina*, (354) *Eleonora*, and (446) *Aeternitas* in the upper focus (e) in Fig. 16. Further characteristic of A-types is a large z_4 score due to the large olivine content, see Fig. 17. Among all classified asteroids, A-types have both the largest z_1 as well as z_4 score. We note that all three spectra of Mars-Crosser (1951) *Lick* are exceptionally red, even among A-types (Brunetto et al. 2007).

32 asteroids (1.5 %) are classified as A-types in this study. They fall into clusters 9, 12, 27, and 49.

4.6.2 O-Types

The class O was introduced in 1993 for supposedly ordinary-chondritic (3628) *Boznemcova* (Binzel et al. 1993). Its noteworthy characteristic is the wide, round $1 \mu\text{m}$ feature as shown in Fig. 15, placing it between the known A-, Q-, and V-types. The albedo is close to the S-complex average at 25 %.

None of the previously classified O-types besides archetype (3628) *Boznemcova* remain as O, and a comparison of these objects in spectral space showed little resemblance. While we assign with (7472) *Kumakiri* a second asteroid to the class, we find in this work that (3628) *Boznemcova* remains without a true spectral sibling. (7472) *Kumakiri* was previously classified as V (Solontoi et al. 2012), however, its spectral resemblance to (3628) *Boznemcova* has been pointed out by Burbine et al. (2011).

The unique appearance of the O-types can be seen by their position in the latent space shown in Figs. 16 and 17. The depth and shape of the $1 \mu\text{m}$ band in combination with the lack of overall slope place the O-types (3628) *Boznemcova* and (7472) *Kumakiri* between the classes Q and V in z_1 - z_2 , refer to the upper focus (a) in Fig. 16, while in z_3 - z_4 , they are closest to A-types.

2 asteroids (0.1 %) are classified as O-types in this study. We debated whether keeping the O-class in the taxonomy is compatible with the overall approach of data-driven clustering. In the end, the unique feature and position of (3628) *Boznemcova* convinced us, however, an argument against single-object classes can be made. The O-class was difficult to carve out from the clusters in the given method. It is derived from a three-component mixture model of the already diffuse cluster 13, which is split into

Table 2: The evolution of the taxonomic scheme from Tholen (1984) over the Bus-DeMeo system to this work. Arrows are used to indicate the overall evolution of each class. The T-class is not present in this taxonomy and the feature characteristic of the Xn has been grouped into the k-feature. The evolution of the X-complex between the taxonomies is unclear as the visual albedo is not taken into account in the Bus-DeMeo system.

Tholen		Bus-DeMeo		This Work
B	→	B	→	B
F	↗			
G	→	Cg	↘	
	→	Cgh	↘	
C	→	C	→	C
	→	Ch	→	Ch
	→	Cb	↗	
D	→	D	→	D
			→	Z
P	...	Xc	...	P
M	...	Xk	...	M
X	...	X	...	X
E	...	Xe	...	E
	...	Xn		
T	→	T		
Q	→	Q		Q
	↗	Sq		
	↗	Sr	↘	
S	→	S	→	S
	↘	Sa	↗	
		Sv		
O	→	O	→	O
R	→	R	→	R
A	→	A	→	A
V	→	V	→	V

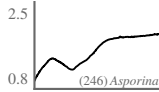
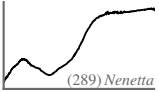
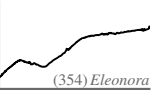
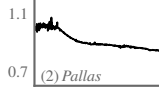
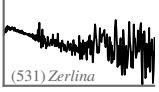
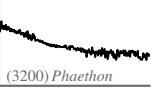
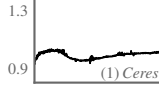
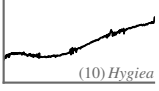
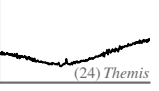
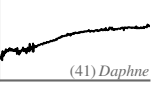
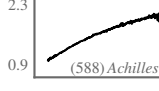
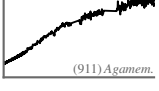
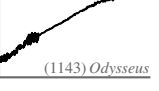
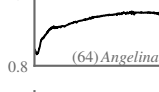
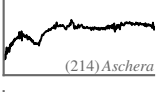
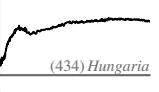
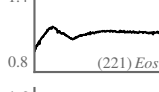
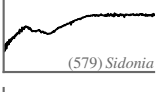
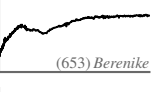
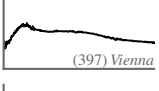
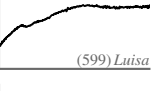
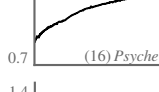
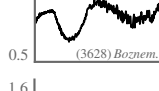
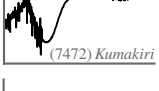
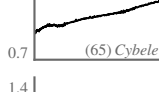
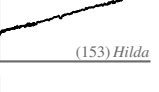
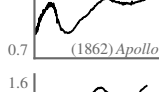
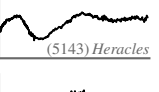
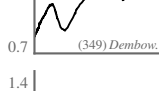
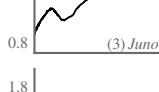
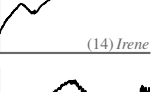
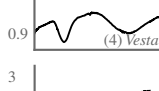
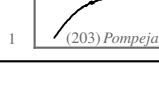
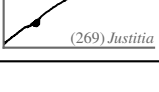
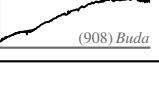
C, O, and Q. Any assignment of the O-class by the classification tool should undergo visual scrutiny and direct comparison to the spectrum of (3628) *Boznemcova*.

4.6.3 R-Types

The R-types are the second niche class of this taxonomy, built around (349) *Dembowska*. The unique nature of (349) *Dembowska* is recognized joint with the one of (4) *Vesta* in early works of taxonomy (Chapman et al. 1975; Zellner and Gradie 1976) and the R-class was introduced in Bowell et al. (1978). However, the A-class which was split off the R-class in Veeder et al. (1983) has since ingested most R-types. The continuity between A and R is visible in Fig. 17.

R-types show $1 \mu\text{m}$ and $2 \mu\text{m}$ features which are deeper than the ones in S-types. The width of the $1 \mu\text{m}$ is between the V- and the Q-types. They have albedos on the upper end of the S-complex distribution, around 28 %, refer to Fig. 15. The spectral appearance is associated to low-iron ordinary chondrites (Zellner and Gradie 1976). We note that of the four samples of (349) *Dembowska* two are classified as R and another two as V, refer to the upper focus (c) in Fig. 16, where we further give the position of R-class member (8693) *Matsuki*.

Table 3: Description of spectral appearance, visual albedo distribution giving the mean value and the lower and upper standard deviation, and spectral prototypes of the 17 classes defined in this taxonomy excluding the X-types.

Class	Spectrum	Albedo	Prototypes		
A	Broad and deep absorption feature at 1 μm , strong red slope in the near-infrared.	0.25 ^{0.09} _{0.07}			
B	Neutral- to blue slope in the visible, blue slope in the near-infrared.	0.06 ^{0.05} _{0.03}			
C	Red visible slope with a possible broad feature around 1 μm and a red near-infrared slope. The spectrum might have an overall concave shape.	0.05 ^{0.02} _{0.01}			
Ch	Absorption feature at 0.7 μm . The near-infrared slope is red while the overall shape might be convex.	0.05 ^{0.02} _{0.01}			
D	Featureless with steep red slope with a possible convex shape longward of 1.5 μm .	0.06 ^{0.03} _{0.02}			
E	Strong red slope in the visible with a feature around 0.9 μm of varying depth and a neutral near-infrared continuation.	0.57 ^{0.15} _{0.12}			
K	Strong red slope in the visible with a broad feature around 1 μm followed by a blue- to neutral near-infrared slope.	0.13 ^{0.04} _{0.03}			
L	Variable appearance apart from a red visible slope. A small feature around 1 μm and a possible one at 2 μm . The near-infrared slope is blue or red.	0.18 ^{0.07} _{0.05}			
M	Linear red slope with possible faint features around 0.9 μm and 1.9 μm . Might show convex shape in the near-infrared.	0.14 ^{0.05} _{0.04}			
O	Broad, bowl-shaped 1 μm absorption feature and a weaker feature at 2 μm .	0.26 ^{0.02} _{0.02}			
P	Linear red slope and generally featureless. Less red than D-types.	0.05 ^{0.02} _{0.01}			
Q	Broad absorption at 1 μm and a shallow feature at 2 μm . An overall blue slope in the near-infrared.	0.24 ^{0.12} _{0.08}			
R	Strong feature at 1 μm and a feature at 2 μm . The latter feature is shallower than in V-types.	0.30 ^{0.05} _{0.04}			
S	Moderate features around 1 μm and 2 μm and a neutral- to red near-infrared slope.	0.24 ^{0.10} _{0.07}			
V	Deep absorption features at 1 μm and 2 μm . The former is much narrower than the latter.	0.29 ^{0.11} _{0.08}			
Z	Extremely red slope, redder than the D-types. Featureless but may exhibit concave shape in the near-infrared.	0.07 ^{0.04} _{0.03}			

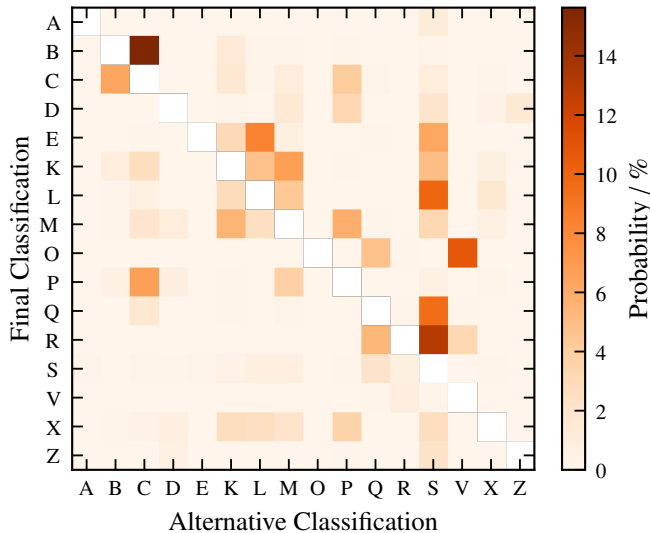


Figure 18: For each class in the taxonomic scheme, we give the average probability of its samples to be classified as any other class based on the complete dataset. Note that the Ch-class is missing as it relies on the detection of the $0.7\ \mu\text{m}$ h-feature and does not have a class probability associated. For better readability, the main matrix diagonal corresponding to the equal-class cases is left empty. These values are generally above 80 % and lowest for K, L, M, and R.

10 asteroids (0.5 %) are classified as R-types in this study. The class is derived from cluster 10 in a two component Gaussian mixture model fit in z_1 - z_2 , where objects with lower z_2 scores are assigned to the S-class.

4.6.4 V-Types

(4) *Vesta* was the first asteroid to be observed spectrophotometrically (McCord et al. 1970) and the V-types have been an established and easily-recognizable class in all asteroid taxonomies since Tholen (1984). They are second class besides S with an established meteoritic analogue, the HED meteorites (e.g. Kelley et al. 2003). The class makes no exception here, its members differentiate easily in both z_2 and z_3 due to the large contribution of pyroxene to the spectral appearance giving rise to the characteristic deep $1\ \mu\text{m}$ and $2\ \mu\text{m}$ features, refer to Figs. 15 to 17. ChangesClass archetype (4) *Vesta* is highlighted in the upper focus (a) in Fig. 16.

The large class variance in z_2 and z_3 represents a high variability in terms of band depth and position in the $0.9\ \mu\text{m}$ - and $2.0\ \mu\text{m}$ -features. However, we do not identify a subpopulation based on the band parameters as was suggested by Binzel and Xu (1993).

142 asteroids (6.7 %) are classified as V-types in this study. V-types populate clusters 7, 15, 18, 28, 32, and 45. V-types with a blue slope in the NIR further share the diffuse cluster 41 with the B-types.

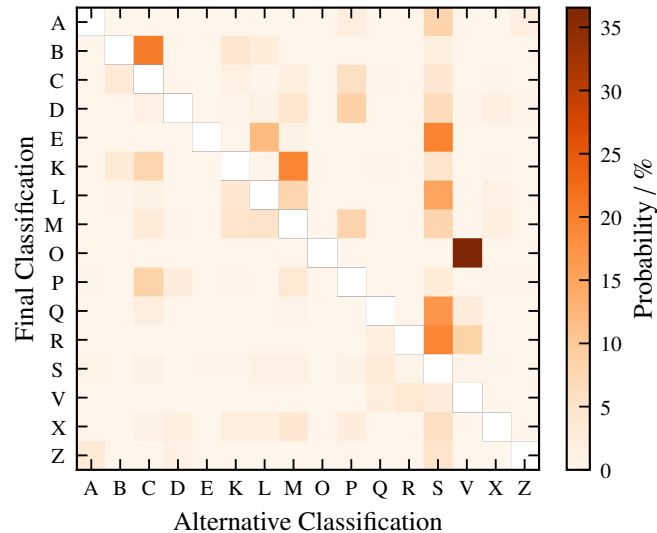


Figure 19: As Fig. 18, using the dataset of 2923 visible-only spectra with 81.4 % albedo observations. Note the difference colourbar scale as in Fig. 18. The main matrix diagonal values are between 63 %–91 % and lowest for K, L, M, and O.

5 CLASSIFICATION

In this section, we introduce the classification tool accompanying this work. We demonstrate the probabilistic classification results using asteroid observations with different wavelength regions covered. We further investigate degeneracies in the classification space. Finally, we compare the results obtained in this taxonomy to the previous systems.

5.1 Classification tool: *classy*

To facilitate the classification of asteroid observations within the framework of this taxonomy, we provide the `classy`¹⁴ (“CLASsification of a Solar System body”) tool written in python. It offers to interactively smooth the input spectral observations prior to resampling them to the required wavelength grid, automatically apply the necessary pre-processing steps outlined in Sect. 2 to both spectra and albedo, identify features in the spectra as outlined in Sect. 3.4.3 (either fully automated or guided by the user), execute the cluster-to-class decision tree and return the probabilistic classifications for each observation.

`classy` provides a command-line interface written in python and is available for Windows, MacOS, and Linux. The software is actively maintained and developed by the authors.

5.2 Class Degeneracies

The probabilistic nature of the classifications in this taxonomy allow to quantify the degeneracies between classes in certain wavelength-regions and in albedo. One example is given in Sect. 4.1.1, where we point out the degeneracy of B and K in the case of a near-infrared-only observation.

We can quantify class degeneracies for two datasets in this work:

¹⁴<https://github.com/maxmahlke/classy>

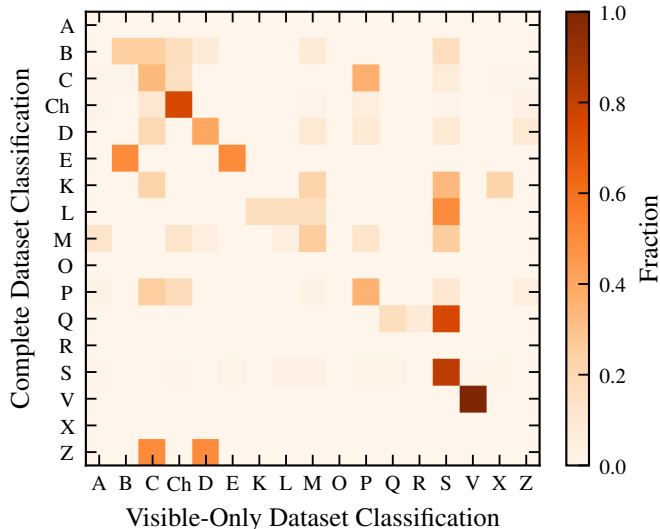


Figure 20: Comparison of the classifications of 328 samples of 267 unique asteroids resulting from visible-only spectra with 81.4 % observed albedos to the classifications of the same asteroids resulting from the complete sample classifications. Note that the sample sizes per row differ: the intersection of asteroids present in both datasets gives 2 samples classified as E using complete samples as well as 2 samples classified as Z, while there are 140 samples entering the calculation in the row of S-types. No A-, O-, or X-types are present in both samples.

the 2983 dataset used to devise the clustering as well as the 2923 visible-only dataset shown in gray in Fig. 1 with 81.4 % albedos observed. We will refer to these samples as the “complete” dataset and the “visible-only” dataset, however, this wording is not entirely accurate as more than 50 % of samples in the complete sample are NIR-only spectra and the visible-only sample contains more than 80 % of albedo observations.

5.2.1 Complete Sample

To estimate the class degeneracy in the complete dataset, we compute for all samples assigned to a given class the average probability to belong to any other class. This comparison is given in Fig. 18. The Ch-class is missing as it relies on the detection of the h-feature and as such does not have a class probability associated. Larger matrix element values indicate a higher degeneracy between the classes. A large sum per matrix row indicates that the class assignment is overall less certain.

Figure 18 shows the intuitive result that endmember classes such as A, V, and Z are assigned with a large probability. The largest degeneracies in pairs of classes are between B- and C-types and R- and S-types. Neither result is surprising as they are overlapping in latent space and even in visual inspection, these classes can be difficult to tell apart. The largest uncertainty overall for a single class (given by the sum per row in Fig. 18) is around 20 % for K, L, and M as well as for the R-types. For the first three, we already pointed out in Sect. 4.3 the similarity in data-space between these classes, hence this result is again expected.

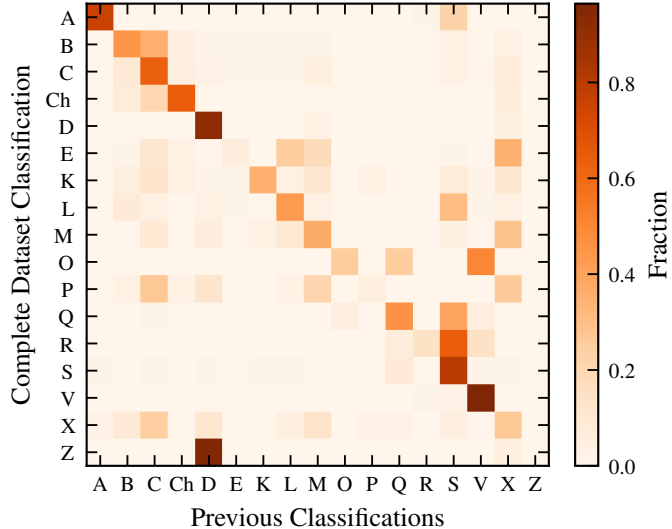


Figure 21: Comparison of the classifications of 2676 samples of 1852 unique asteroids classified in the complete dataset to the classifications in the literature. The literature classifications were mapped into this taxonomy scheme following Table 2. Note that the number of samples per row differs.

5.2.2 Visible-Only Sample

The estimation of the class degeneracy is repeated for the visible-only dataset after classifying the samples therein using the `classy` tool. Figure 19 shows a similar result as for the complete dataset, only that the overall values of uncertainty increase. Instead of 80 %–99 % certainty in the class assignment, we here get values between 63 %–91 %. Besides this overall change in scale, we do not observe significant differences between the results for the visible-only dataset and the complete one. K, L, and M remain among the least-certain classes, while O-types have the largest uncertainty due to the missing 1 μm -band.

5.2.3 Complete versus Visible-Only Sample

Another way to investigate class degeneracies is the comparison of classifications resulting from samples with different wavelength-regions observed. 267 asteroids are present in both the complete and the visible-only datasets with a total of 328 observations. For these asteroids, we compare the resulting classifications based on the samples in both datasets, shown in Fig. 20. Each row gives for each class in the taxonomy the fraction of asteroids classified as any class based on the visible-only dataset. Note that the figure does not account for the different samples sizes: there are 2 samples classified as E in the intersection of the dataset and 140 classified as S. No samples classified as A, O, and X are present in both samples.

Figure 20 shows that Ch, S, and V are the most reliable when classified using visible-only data. Ch benefits from the binary classification which takes place once the h-feature is observed. The members of the M-complex show increasing degeneracy with the S-class with decreasing near-infrared coverage. The least-expected degeneracies are Z and C as well as E and B, however, both are based on a single sample.

Both results in Figs. 19 and 20 show that visible-only spectra in combination with the albedo place a strong constraint on the taxonomic class, as is well-established from the previous taxonomies which relied on the visible wavelength ranges exclusively. This highlights the strengths of the new method employed here: NIR are not strictly necessary to derive a classification as incomplete observations can be classified and the albedo as an accessible observable is accounted for.

5.3 Comparison to previous taxonomies

Class continuity was one of the aspects which we considered when designing the scheme of classes in this taxonomy. We quantify this goal as above using a confusion matrix, only that we compare the classes assigned based on the complete dataset to the most-probable previous classification of the asteroid in the literature, retrieved for 2676 samples of 1852 unique asteroids from the SsODNet database. We convert the previous classifications done mostly in the Bus-DeMeo scheme to this scheme using the mapping given in Table 2.

Figure 21 shows an overall good agreement of the classes assigned in this work with the ones from the literature. Notable exceptions are the 0-type, which has no legacy members apart from (3628) *Boznemcova* as pointed out in Sect. 4.6.2, and the novel Z-class, which hosts almost exclusively previous D-type. Furthermore, the L loses members to the S as well as 0 to V.

6 CONCLUSION

The taxonomic scheme for minor body classification has been developed for close to 50 years. During this time, numerous efforts to categorize the observational properties of asteroids have been driven forward through dedicated observational campaigns and instrumental advancement. We focused on the methodology and statistical foundation, allowing us to increase the sample size by an order of magnitude compared to the previous taxonomy by DeMeo et al. (2009) and to re-introduce the albedo into the classifying observables as done in Tholen (1984).

The dimensionality reduction and clustering applied to 2983 spectra of 2125 asteroids revealed three main complexes: the well established C- and S-complexes and a restructured M-complex. While the S-complex is well understood in terms of mineralogy and meteoritic analogue material, both the C-complex and M-complex show a large degree of variability of so far unknown origin. We derive 17 classes from the three complexes, where the data-driven clustering is guided by the previous taxonomies and the goal of class continuity.

A classification tool named `cLassy` is available online and allows the user to classify asteroid observations covering the spectral VisNIR region and the visual albedo either completely or partially. The resulting array of class probabilities for each sample serves to estimate classification uncertainty and possible taxonomic trends.

We have established a methodology for asteroid taxonomy which is well suited for the current and future datasets of asteroid observations. The on-going MITHNEOS survey (Binzel et al. 2019), the upcoming Gaia Data Release 3 (including visible spectra, Delbo et al. 2012), and the SPHEREx survey (Ivezić et al. 2022) will provide or continue to provide spectral observations of asteroids in different wavelengths, which are able to be classified

within the framework of this taxonomy.

The dimensionality reduction and clustering are able to resolve more features and find more meaningful clusters when fed with more data. As such, it may be worthwhile exploring how the model properties described in Sect. 3 change when fed with significantly more data. Nevertheless, during this work, we have noticed that the latent space properties show little change whether we train with 500, 1000, or all samples in the dataset. Instead, we anticipate that a future taxonomy-revision will benefit more from an increased feature-set. In particular the ultra-violet information offered by the Gaia data may solve degeneracies in the C- and M-complex. A further improvement should be the addition of polarimetric data, provided the amount of observations is comparable to the availability of the other features. The M-complex could benefit, and we consider that most work is left to be done in this complex. Extension of the spectral space into the 3 μm region is promising as well.

ACKNOWLEDGEMENTS

The authors thank the numerous members of the community who shared their spectral observations of minor bodies to support this work. Rémi Flamary provided valuable support in the exploration of machine learning methods during the initial stage of the project.

This research has made use of IMCCE’s SsODNet/Quaero VO tool.

This research has made use of IMCCE’s Miriade VO tool.

This research has made use of the SVO Filter Profile Service supported from the Spanish MINECO through grant AYA2017-84089.

All (or part) of the data utilized in this publication were obtained and made available by the MITHNEOS MIT-Hawaii Near-Earth Object Spectroscopic Survey. The IRTF is operated by the University of Hawaii under contract 80HQTR19D0030 with the National Aeronautics and Space Administration. The MIT component of this work is supported by NASA grant 80NSSC18K0849.

Malheureusement, la nature de l’astéroïde B612 reste un mystère.

REFERENCES

- Abadi, M. et al. (2015). TensorFlow: Large-Scale Machine Learning on Heterogeneous Systems. misc. Software available from tensorflow.org.
- Alí-Lagoa, V. et al. (2016). *Astronomy & Astrophysics* 591, A14.
- Baek, J., McLachlan, G. J., and Flack, L. K. (2010). *IEEE Transactions on Pattern Analysis and Machine Intelligence* 32 (7), 1298–1309.
- Bell, J. F. (1988). *Meteoritics* 23, 256–257.
- Bell, J. F., Davis, D. R., Hartmann, W. K., and Gaffey, M. J. (1989). Asteroids: the big picture. In: *Asteroids II*. Ed. by R. P. Binzel, T. Gehrels, and M. S. Matthews, 921–945.
- Binzel, R. P. et al. (2019). *Icarus* 324, 41–76.
- Binzel, R. P. and Xu, S. (1993). *Science* 260 (5105), 186–191.
- Binzel, R. P. et al. (1993). *Science* 262 (5139), 1541–1543.
- Binzel, R. P. et al. (2004). *Icarus* 170 (2), 259–294.

- Bottke, W. F., Nesvorný, D., Grimm, R. E., Morbidelli, A., and O'Brien, D. P. (2006). *Nature* 439 (7078), 821–824.
- Bouveyron, C., Celeux, G., Murphy, T. B., and Raftery, A. E. (2019). *Model-Based Clustering and Classification for Data Science: With Applications in R*. Cambridge Series in Statistical and Probabilistic Mathematics. Cambridge.
- Bowell, E., Chapman, C. R., Gradie, J. C., Morrison, D., and Zellner, B. (1978). *Icarus* 35.3, 313–335.
- Brunetto, R., León, J. de, and Licandro, J. (2007). *Astronomy & Astrophysics* 472 (2), 653–656.
- Brunetto, R. and Strazzulla, G. (2005). *Icarus* 179 (1), 265–273.
- Brunetto, R. et al. (2006). *Icarus* 184 (2), 327–337.
- Burbine, T. H., Duffard, R., Buchanan, P. C., Cloutis, E. A., and Binzel, R. P. (2011). Spectroscopy of O-Type Asteroids. In: *42nd Annual Lunar and Planetary Science Conference*. Lunar and Planetary Science Conference, 2483.
- Burbine, T. H., McCoy, T. J., Meibom, A., Gladman, B., and Keil, K. (2002). Meteoritic Parent Bodies: Their Number and Identification. In: *Asteroids III*, 653–667.
- Bus, S. J. and Binzel, R. P. (2002a). *Icarus* 158 (1), 106–145.
- Bus, S. J. and Binzel, R. P. (2002b). *Icarus* 158 (1), 146–177.
- Candolle, A. P. d. (1813). Exposition des principes de la classification naturelle et de l'art de décrire et d'étudier les végétaux. In: *Théorie élémentaire de la botanique*.
- Carry, B. (2012). *Planetary and Space Science* 73 (1), 98–118.
- Carvano, J. M., Hasselmann, P. H., Lazzaro, D., and Mothé-Diniz, T. (2010). *Astronomy and Astrophysics* 510, A43.
- Casey, A. R. et al. (2019). *The Astrophysical Journal* 887 (1), 73.
- Cellino, A., Bagnulo, S., Tanga, P., Novaković, B., and Delbò, M. (2014). *Monthly Notices of the Royal Astronomical Society: Letters* 439 (1), L75–L79.
- Chapman, C. R., Johnson, T. V., and McCord, T. B. (1971). A Review of Spectrophotometric Studies of Asteroids. In: *NASA Special Publication*. Ed. by T. Gehrels. 267, 51.
- Chapman, C. R., Morrison, D., and Zellner, B. (1975). *Icarus* 25 (1), 104–130.
- Chrbolková, K. et al. (2021).
- Clark, B. E., Bus, S. J., Rivkin, A. S., Shepard, M. K., and Shah, S. (2004). *The Astronomical Journal* 128 (6), 3070–3081.
- Clark, B. E. et al. (2009). *Icarus* 202 (1), 119–133.
- Clark, B. E. et al. (2010). *Journal of Geophysical Research (Planets)* 115.E6, E06005, E06005.
- Cloutis, E., Hudon, P., Hiroi, T., Gaffey, M., and Mann, P. (2011). *Icarus* 216 (1), 309–346.
- Cloutis, E. A., Gaffey, M. J., Smith, D. G. W., and Lambert, R. S. J. (1990a). *Journal of Geophysical Research* 95 (B6), 8323.
- Cloutis, E. A., Gaffey, M. J., Smith, D. G. W., and Lambert, R. S. J. (1990b). *Journal of Geophysical Research* 95 (B1), 281.
- Cruikshank, D. P. and Hartmann, W. K. (1984). *Science* 223 (4633), 281–283.
- De Sanctis, M. C. et al. (2015). *Nature* 528 (7581), 241–244.
- Delbo, M. et al. (2012). *Planetary and Space Science* 73 (1), 86–94.
- DeMeo, F. E. and Carry, B. (2013). *Icarus* 226 (1), 723–741.
- DeMeo, F. E. and Carry, B. (2014). *Nature* 505.7485, 629–634.
- DeMeo, F. E., Binzel, R. P., Carry, B., Polishook, D., and Moskovitz, N. A. (2014). *Icarus* 229, 392–399.
- DeMeo, F. E., Binzel, R. P., Slivan, S. M., and Bus, S. J. (2009). *Icarus* 202 (1), 160–180.
- DeMeo, F. E. et al. (2019). *Icarus* 322, 13–30.
- Dempster, A. P., Laird, N. M., and Rubin, D. B. (1977). *Journal of the Royal Statistical Society. Series B (Methodological)* 39.1, 1–38.
- Devogèle, M. et al. (2018). *Icarus* 304, 31–57.
- Devogèle, M. et al. (2019). *The Astronomical Journal* 158 (5), 196.
- Eschrig, J., Bonal, L., Beck, P., and Prestgard, T. (2021). *Icarus* 354, 114034.
- Fornasier, S., Lantz, C., Barucci, M., and Lazzarin, M. (2014). *Icarus* 233, 163–178.
- Fornasier, S. et al. (2010). *Icarus* 210 (2), 655–673.
- Gaffey, M. J. and McCord, T. B. (1979). Mineralogical and petrological characterizations of asteroid surface materials. In: *Asteroids*. Ed. by T. Gehrels and M. S. Matthews, 688–723.
- Gaffey, M. J., Reed, K. L., and Kelley, M. S. (1992). *Icarus* 100 (1), 95–109.
- Gomes, R., Levison, H. F., Tsiganis, K., and Morbidelli, A. (2005). *Nature* 435 (7041), 466–469.
- Gradie, J. and Tedesco, E. (1982). *Science* 216.4553, 1405–1407.
- Granvik, M. and Brown, P. (2018). *Icarus* 311, 271–287.
- Hanuš, J. et al. (2017). *Astronomy & Astrophysics* 601, A114.
- Hardersen, P., Gaffey, M., and Abell, P. (2005). *Icarus* 175 (1), 141–158.
- Harris, A. W. and Lagerros, J. S. V. (2002). Asteroids in the Thermal Infrared. In: *Asteroids III*, 205–218.
- Hasegawa, S. et al. (2021). *The Astrophysical Journal Letters* 916.1, L6.
- Hiroi, T., Zolensky, M. E., Pieters, C. M., and Lipschutz, M. E. (1996). *Meteoritics & Planetary Science* 31 (3), 321–327.
- Ivezić, Ž. et al. (2022). *Icarus* 371, 114696.
- Kelley, M. S., Vilas, F., Gaffey, M. J., and Abell, P. A. (2003). *Icarus* 165 (1), 215–218.
- Lantz, C., Binzel, R., and DeMeo, F. (2018). *Icarus* 302, 10–17.
- Lantz, C. et al. (2017). *Icarus* 285, 43–57.
- Lazzaro, D. et al. (2004). *Icarus* 172 (1), 179–220.
- León, J. de, Pinilla-Alonso, N., Campins, H., Licandro, J., and Marzo, G. (2012). *Icarus* 218 (1), 196–206.
- Little, R. and Rubin, D. (2019). *Wiley Series in Probability and Statistics*.
- Mahlke, M., Carry, B., and Denneau, L. (2021). *Icarus* 354, 114094.
- Marsset, M. et al. (2016). *A&A* 586, A15, A15.
- Masiero, J. R., DeMeo, F. E., Kasuga, T., and Parker, A. H. (2015). Asteroid Family Physical Properties. In: *Asteroids IV*.
- Masiero, J. R. et al. (2011). *The Astrophysical Journal* 741.2, 68.
- McCord, T. B., Adams, J. B., and Johnson, T. V. (1970). *Science* 168 (3938), 1445–1447.
- McCord, T. B. and Chapman, C. R. (1975). *The Astrophysical Journal* 195, 553.
- Montanari, A. and Viroli, C. (2010). *Statistical Modelling* 10 (4), 441–460.
- Morbidelli, A., Levison, H. F., Tsiganis, K., and Gomes, R. (2005). *Nature* 435 (7041), 462–465.
- Morbidelli, A., Walsh, K. J., O'Brien, D. P., Minton, D. A., and Bottke, W. F. (2015). The Dynamical Evolution of the Asteroid Belt. In: *Asteroids IV*.
- Mothé-Diniz, T., Carvano, J., Bus, S., Duffard, R., and Burbine, T. (2008). *Icarus* 195 (1), 277–294.
- Mueller, B. E., Tholen, D. J., Hartmann, W. K., and Cruikshank, D. P. (1992). *Icarus* 97 (1), 150–154.
- Nakamura, T. et al. (2011). *Science* 333 (6046), 1113–1116.
- Neeley, J. et al. (2014). *Icarus* 238, 37–50.

- Ockert-Bell, M. et al. (2010). *Icarus* 210 (2), 674–692.
- Pearson, K. (1901). The London, Edinburgh, and Dublin philosophical magazine and journal of science 2.11, 559–572.
- Popescu, M. et al. (2018). *Astronomy & Astrophysics* 617, A12.
- Ribeiro de Sousa, R. et al. (2022). *Icarus*, 114933.
- Rivkin, A. S. (1995). *Icarus* 117 (1), 90–100.
- Rivkin, A. S. (2000). *Icarus* 145 (2), 351–368.
- Rivkin, A. S. (2012). *Icarus* 221 (2), 744–752.
- Rivkin, A. S., Thomas, C. A., Howell, E. S., and Emery, J. P. (2015). *The Astronomical Journal* 150 (6), 198.
- Rubin, D. B. and Thayer, D. T. (1982). *Psychometrika* 47 (1), 69–76.
- Sanchez, J. A. et al. (2012). *Icarus* 220.1, 36–50.
- Savitzky, A. and Golay, M. J. E. (1964). *Analytical Chemistry* 36, 1627–1639.
- Shepard, M. K. et al. (2008). *Icarus* 193 (1), 20–38.
- Shepard, M. K. et al. (2010). *Icarus* 208 (1), 221–237.
- Shepard, M. K. et al. (2015). *Icarus* 245, 38–55.
- Shestopalov, D., Golubeva, L., McFadden, L., Fornasier, S., and Taran, M. (2010). *Planetary and Space Science* 58 (10), 1400–1403.
- Shevchenko, V. G. et al. (2016). *Planetary and Space Science* 123 (None), 101–116.
- Solontoi, M. R., Hammergren, M., Gyuk, G., and Puckett, A. (2012). *Icarus* 220 (2), 577–585.
- Strazzulla, G. et al. (2005). *Icarus* 174 (1), 31–35.
- Sunshine, J. M., Connolly, H. C., McCoy, T. J., Bus, S. J., and La Croix, L. M. (2008). *Science* 320 (5875), 514–517.
- Tedesco, E. F., Noah, P. V., Noah, M., and Price, S. D. (2002). *The Astronomical Journal* 123 (2), 1056–1085.
- Tholen, D. J. and Barucci, M. A. (1989). Asteroid taxonomy. In: *Asteroids II*. Ed. by R. P. Binzel, T. Gehrels, and M. S. Matthews, 298–315.
- Tholen, D. J. (1984). Asteroid Taxonomy from Cluster Analysis of Photometry. PhD Thesis. University of Arizona, Tucson.
- Thomas, C. A., Trilling, D. E., and Rivkin, A. S. (2012). *Icarus* 219 (1), 505–507.
- Thomas, C. A., Trilling, D. E., Rivkin, A. S., and Linder, T. (2021). *The Astronomical Journal* 161 (3), 99.
- Tipping, M. E. and Bishop, C. M. (1999). *Journal of the Royal Statistical Society: Series B (Statistical Methodology)* 61.3, 611–622.
- Trilling, D. E. et al. (2016). *The Astronomical Journal* 152 (6), 172.
- Tsiganis, K., Gomes, R., Morbidelli, A., and Levison, H. F. (2005). *Nature* 435 (7041), 459–461.
- Usui, F. et al. (2011). *Publications of the Astronomical Society of Japan* 63 (5), 1117–1138.
- Veeder, G., Matson, D., and Tedesco, E. (1983). *Icarus* 55 (1), 177–180.
- Vernazza, P. et al. (2011). *Icarus* 216 (2), 650–659.
- Vernazza, P. et al. (2014). *The Astrophysical Journal* 791 (2), 120.
- Vernazza, P. et al. (2015). *The Astrophysical Journal* 806.2, 204.
- Vernazza, P. et al. (2017). *The Astronomical Journal* 153 (2), 72.
- Vernazza, P. et al. (2021). *Astronomy & Astrophysics* 654, A56.
- Viiikinkoski, M., Hanuš, J., Kaasalainen, M., Marchis, F., and Ďurech, J. (2017). *Astronomy & Astrophysics* 607, A117.
- Vokrouhlický, D., Bottke, W. F., and Nesvorný, D. (2016). *The Astronomical Journal* 152.2, 39.
- Warren, P. H. (2011). *Earth and Planetary Science Letters* 311 (1-2), 93–100.
- Watters, T. R. and Prinz, M. (1979). Lunar and Planetary Science Conference Proceedings 1, 1073–1093.
- Wright, E. L., Mainzer, A., Masiero, J., Grav, T., and Bauer, J. (2016). *The Astronomical Journal* 152 (4), 79.
- Xu, S., Binzel, R. P., Burbine, T. H., and Bus, S. J. (1995). *Icarus* 115 (1), 1–35.
- Yang, B. et al. (2016). *The Astrophysical Journal* 820 (2), L35.
- Zellner, B. and Gradie, J. (1976). *AJ* 81, 262–280.
- Zellner, B., Tholen, D., and Tedesco, E. (1985). *Icarus* 61 (3), 355–416.

A DISTRIBUTION OF ALBEDOS IN CLUSTER

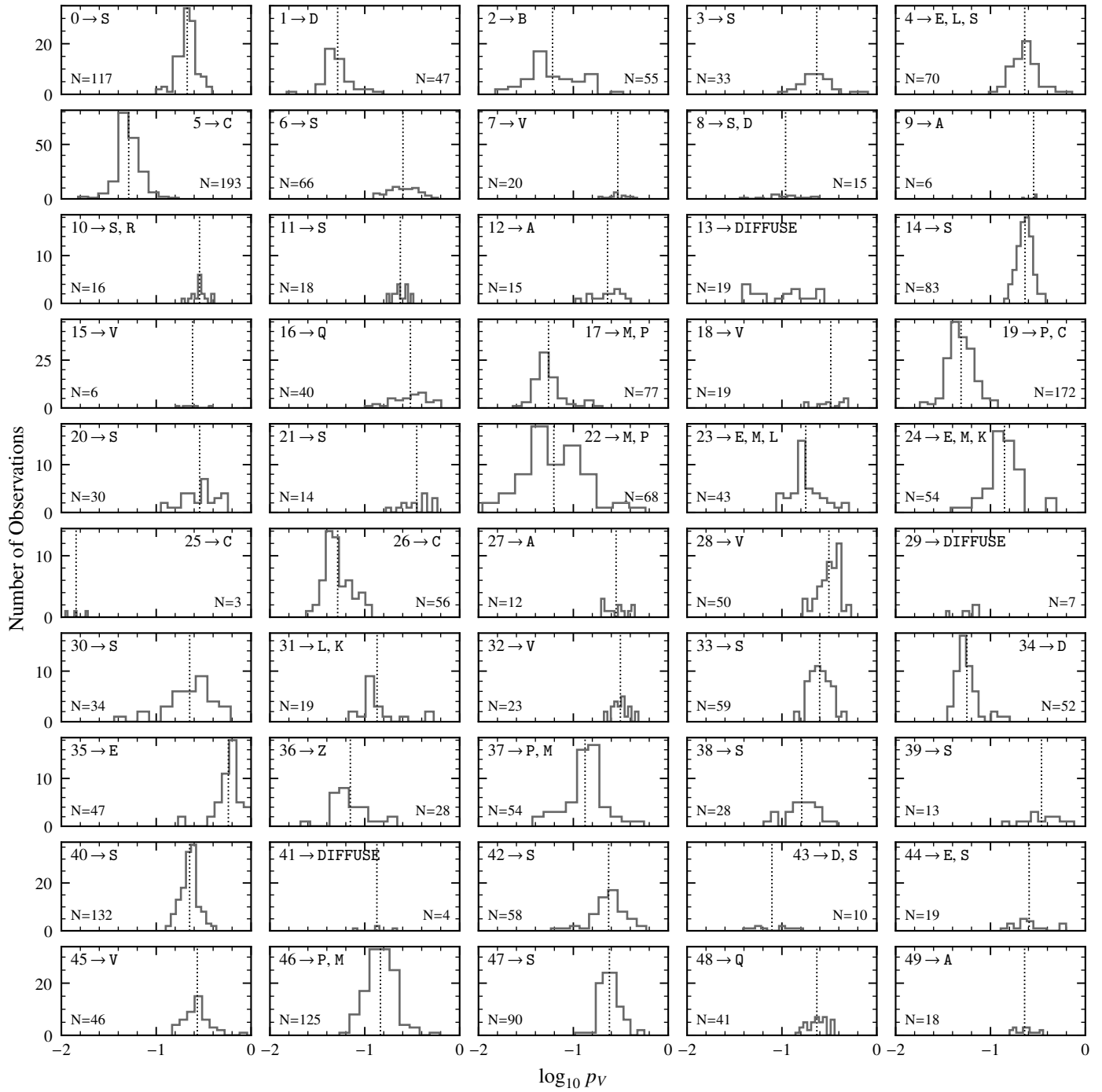


Figure A.1: Overview of the albedo distribution per cluster, including the number N of albedos and the asteroid classes to which the cluster contributes to, excluding classes with fewer than 3 contributed observations except for cluster 25 which has only three observations. The classes are sorted by the total number of observations the cluster contributed. Dotted line gives the mean value of the albedos per cluster except for diffuse clusters and cluster 25. Note the change in y-axis limits per row.

B FEATURE CENTERS AND WINDOWS

Table B.1: Given are the mean band centers and the mean upper and lower band limits determined using the visually-identified features in the input data. These values are applied when using the automatic feature detection with the `classy` tool.

Feature	Center / μm	Lower Limit / μm	Upper Limit / μm
e	0.50 ± 0.01	0.450	0.539
h	0.69 ± 0.01	0.549	0.834
k	0.91 ± 0.02	0.758	1.060

C DISTRIBUTION OF SPECTRA AND ALBEDOS IN CLASSES

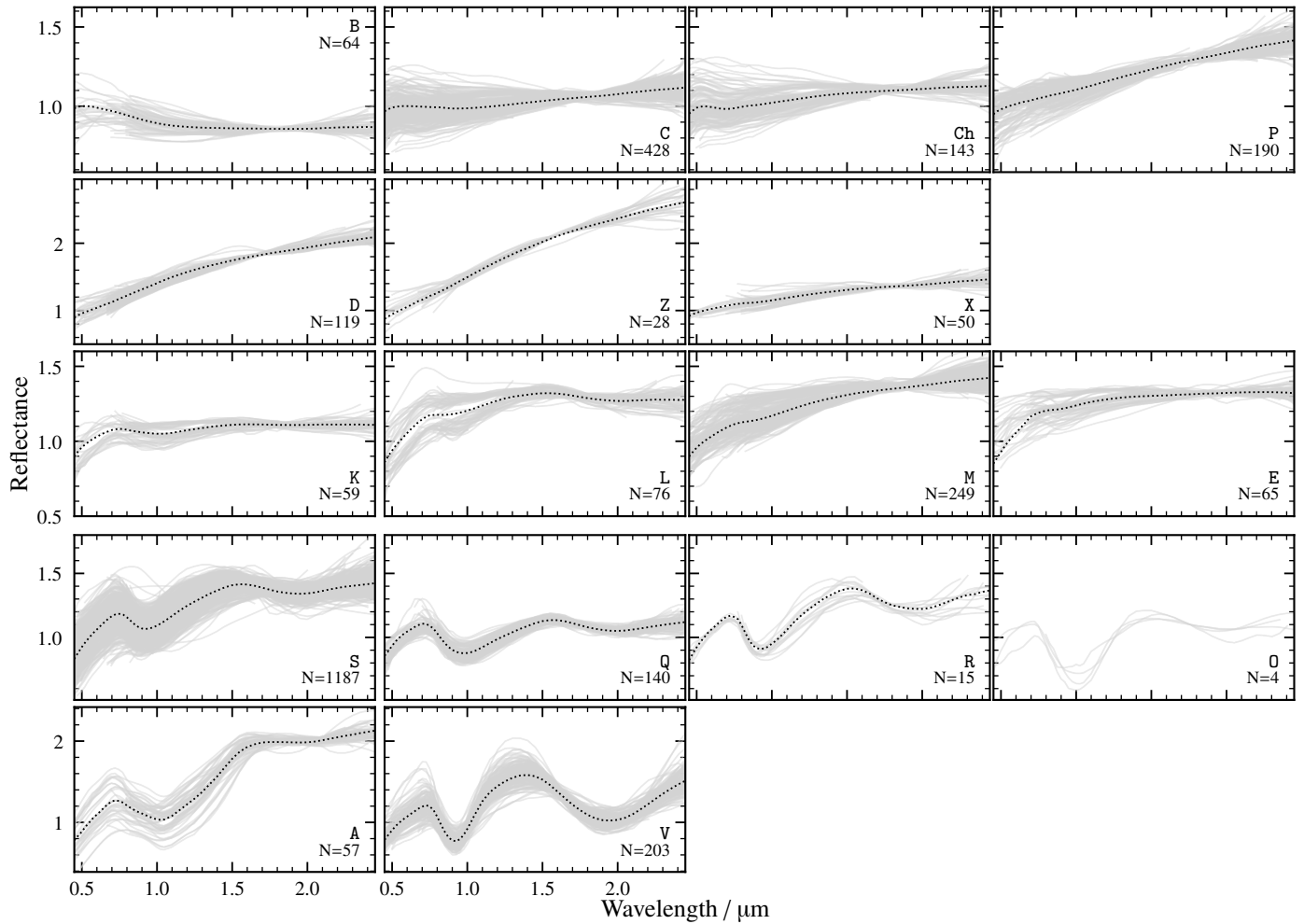


Figure C.2: The distribution of spectral observations over the 17 classes assigned in this taxonomy. The number N of spectral observations assigned to the class is given under the respective letter. Spectra contributed by diffuse clusters are excluded.

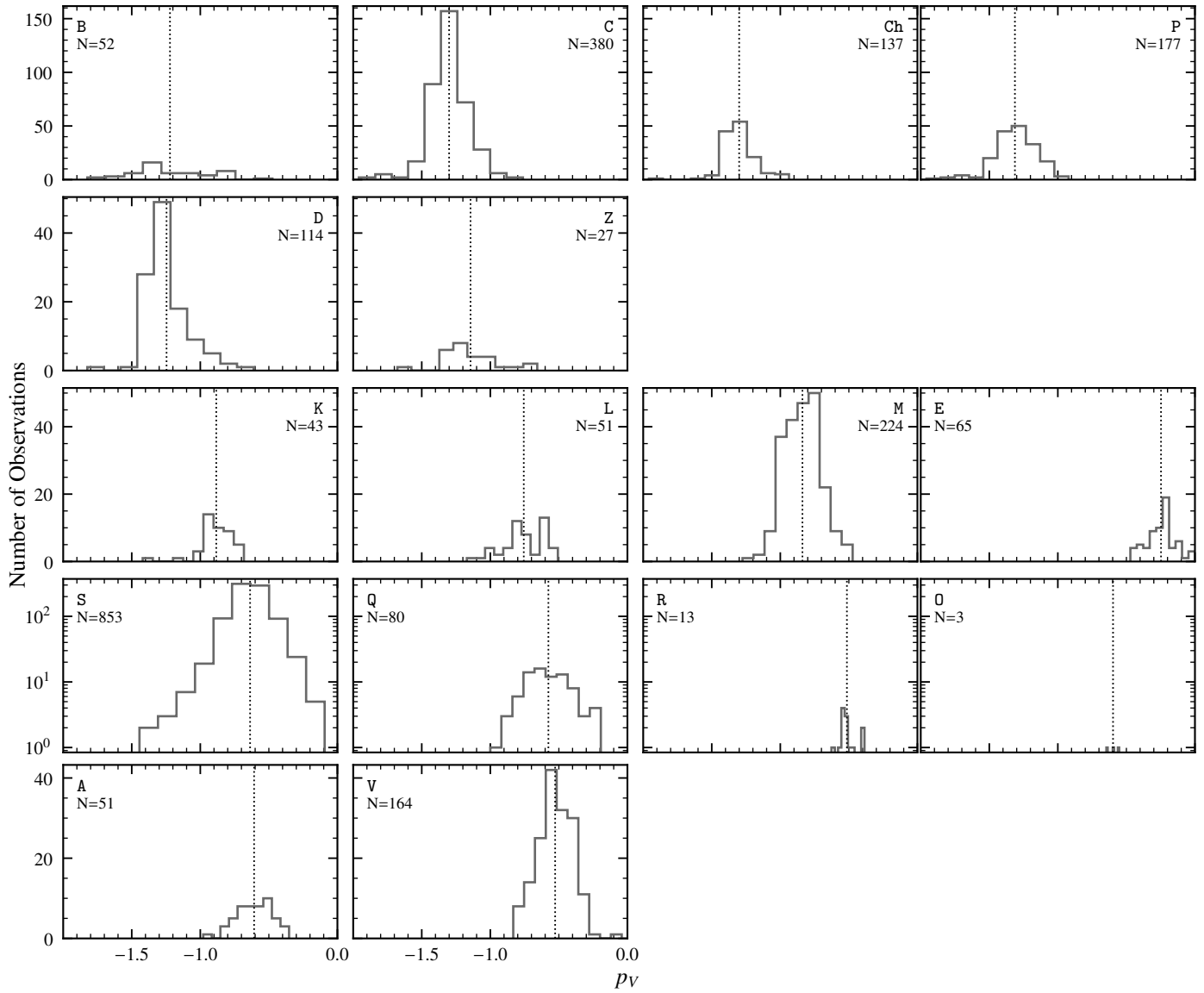


Figure C.3: The distribution of albedo observations over the 17 classes assigned in this taxonomy excluding the X-class. The number N of albedo observations assigned to the class is given under the respective letter. Albedos contributed by diffuse clusters are excluded.